sustainable chemistry

MDPI

Review

Anthracene and Phenanthrene Photocatalytic Degradation in the Presence of Various Types of Metal Oxide Nanocomposites

Vladan Nedelkovski *, Milan Radovanović and Slađana Alagić

Technical Faculty in Bor, University of Belgrade, Vojske Jugoslavije 12, 19210 Bor, Serbia; mradovanovic@tfbor.bg.ac.rs (M.R.); salagic@tfbor.bg.ac.rs (S.A.)
* Correspondence: vnedelkovski@tfbor.bg.ac.rs

Abstract

The persistence and hazardous potential of polycyclic aromatic hydrocarbons (PAHs), with compounds such as anthracene and phenanthrene, raise significant concerns about human health and environmental safety. PAHs are ubiquitous environmental pollutants originating from natural processes and anthropogenic activities, notably fossil fuel combustion. Due to their stability, they tend to accumulate in ecosystems, posing risks to wildlife and human health through bioaccumulation and potential carcinogenicity. Conventional remediation techniques, such as physical adsorption and biological treatment, often fall short in their efficiency and long-term sustainability. Thus, there is an urgent need for innovative methods that can effectively degrade these persistent organic pollutants. Here, we reviewed recent advancements in the photocatalytic degradation of anthracene and phenanthrene, with a focus on metal oxide-based nanocomposites. The major points were: (1) Metal oxides such as TiO_2, ZnO, and CuO, recognized for their photocatalytic properties (they show significantly enhanced efficiency when utilized as a part of nanocomposites, primarily due to the improved charge separation, increased surface area, and numerous active sites); (2) The review of the photocatalytic mechanisms involved in PAH degradation, particularly through the generation of reactive oxygen species that can break down anthracene and phenanthrene into less harmful compounds; and (3) The insights into the formed intermediates and reaction pathways, which can help to deepen the understanding of PAH breakdown and support the design of more efficient catalytic systems for future environmental remediation applications.

Keywords: degradation mechanisms; anthracene; phenanthrene; nanomaterials; photocatalysis

Check for updates

Academic Editor: Francesca Deganello

Received: 28 February 2026
Revised: 19 April 2026
Accepted: 20 April 2026
Published: 3 May 2026

Copyright: © 2026 by the authors. Licensee MDPI, Basel, Switzerland. This article is an open access article distributed under the terms and conditions of the Creative Commons Attribution (CC BY) license.

1. Introduction

Anthracene and phenanthrene, well-known compounds in the group of polycyclic aromatic hydrocarbons (PAHs), pose significant environmental hazards due to their persistence and toxicological effects. These compounds are ubiquitous in the environment, stemming from both natural and anthropogenic processes (mostly fossil fuel combustion and industrial discharges) [1–3]. Their stability enables their accumulation in ecosystems, posing threats to wildlife and human health and complicating their removal from contaminated sites [4,5]. Research indicates that 16 PAHs are among the most hazardous substances to human health and environmental safety [1].

Although anthracene itself has no acute toxicity or carcinogenic risks and is not known to be mutagenic, it can still pose significant health risks. Specifically, chronic exposure has the potential to harm both the hematopoietic and lymphoid systems and may also

trigger allergic reactions in the skin [6]. The Maximum Permissible Concentration (MPC) for anthracene is established at 0.023 micrograms per liter (μg/L) for both freshwater and marine environments. It defines the level below which no detrimental effects on ecosystems are anticipated (over annual averages). Additionally, the Maximum Acceptable Concentration (MAC) of anthracene, aimed at safeguarding aquatic ecosystems from short-term exposure peaks, is set at 0.23 μg/L. MPC of phenanthrene is set at 1.1 micrograms per liter for freshwater, groundwater, and saltwater. MAC of phenanthrene, designed to protect ecosystems from short-term peak concentrations, is set at 6.7 micrograms per liter for both types of water [7,8]. According to the United States Environmental Protection Agency (USEPA), anthracene is not classified as a carcinogen and therefore does not have applicable screening levels for carcinogenic risk in defined Regional Screening Levels (RSLs). For non-carcinogenic risk, i.e., target hazard quotient (THQ) at the level: THQ = 1.0, the allowable concentration for oral ingestion is 6000 μg/L, while the dermal exposure limit is 2500 μg/L. Inhalation is not quantified for non-carcinogenic effects, and the overall non-carcinogenic screening level for cumulative exposure is 1800 μg/L. These thresholds guided the assessment of environmental health risks associated with anthracene exposure in the residents' tap water. USEPA did not define specific screening levels for phenanthrene [9].

More detailed, according to the USEPA, anthracene belongs to Group D: "not classifiable as to human carcinogenicity" (based on the absence of human data and the inadequacy of animal bioassays, which failed to demonstrate statistically significant tumorigenic effects in both: rats and mice, across a range of experimental designs, including dietary exposure and skin-painting assays) [10]. Similarly, phenanthrene is also designated as Group D (according to a lack of epidemiological data and inconclusive animal studies, with only limited tumor-initiating activity observed in a single dermal promotion assay in mice) [11]. Although some in vitro mutagenicity assays, such as those involving *Salmonella typhimurium* and human lymphoblastoid TK6 cells, have yielded positive results for both compounds, the overall weight of evidence remains insufficient to confirm a carcinogenic hazard under current exposure scenarios [10,11].

In response to these concerns, advanced oxidation processes (AOPs), particularly photocatalysis using metal oxides, have emerged as a promising technology for the degradation of PAHs. For instance, zinc oxide (ZnO) and similar materials such as titanium dioxide (TiO_2), and copper oxides (CuO and Cu_2O) are widely recognized for their photocatalytic capabilities [12–15]. These materials can harness solar energy to generate reactive species that effectively degrade PAHs, transforming them into less complex and less harmful substances [16]. Among the available wastewater treatment strategies, heterogeneous photocatalysis is considered to offer both high efficiency and economic benefits (due to the potential for complete mineralization), potentially outperforming alternatives such as ozonation or chlorination. In contrast, chlorination carries the additional risk of generating carcinogenic organochlorine byproducts. Nanofiltration, while sometimes proposed, is regarded as exceedingly expensive, tends to relocate plastic nanoparticles rather than remove them simply, and is susceptible to filter fouling [17].

The role of nanocomposites that incorporate ZnO and other similar metal oxides is particularly significant in the field of photocatalysis [12,18]. These nanocomposites enhance photocatalytic efficiency through improved charge carrier separation, increased surface area, and the availability of more active sites for catalytic reactions [19–21]. The nanocomposite approach addresses the primary limitations of traditional photocatalytic materials, such as the rapid recombination of photoinduced electrons (e^-) and holes (h^+), and limited absorption of visible light [21,22].

Photocatalytic reactions generally encompass three fundamental stages. Initially, during the light absorption phase, semiconductor photocatalysts exposed to sunlight

absorb photons, whose energy matches or exceeds the semiconductor's optical bandgap (Eg). This absorption results in the excitation of electrons from the valence band (VB) to the conduction band (CB), creating electron-hole pairs, or charge carriers. Subsequently, in the charge separation and transfer phase, these charge carriers migrate to the surface of the photocatalyst. In the final phase, surface reactions occur, where the photogenerated electrons and holes engage in redox reactions with substances adsorbed on the catalyst's surface [23,24].

Furthermore, not all electron-hole pairs can recombine immediately; some reach the catalyst surface, where they react with hydroxyl groups (OH), water (H_2O), or oxygen. These interactions produce highly reactive species such as hydroxyl radicals ($^{\bullet}OH$) or superoxide free radicals, which possess the necessary reactivity to break various bonds (C–C, C=C, and C=O) in organic pollutants. This breakdown process may ultimately result in the formation of carbon dioxide (CO_2), water (H_2O), or some other inorganic compounds [25].

Recent advances have focused on the development and synthesis of these nanocomposites, exploring the incorporation of dopants, the creation of heterojunctions, and composite formulations to optimize photocatalytic activity [23,26,27]. Operational parameters such as nanosized photocatalyst composition, pH, catalyst loading, light intensity, and presence of electron acceptors are critically analyzed to maximize the degradation efficiency [28–32]. Studies have shown that there is an optimal photocatalyst loading beyond which the efficiency does not increase due to light scattering and reduced light penetration [33,34]. Advanced oxidation processes (such as UV-activated peroxydisulfate, PDS) have been evaluated for their efficacy in degrading these compounds. Studies have shown that, under these conditions, anthracene degrades more rapidly than phenanthrene, but both compounds can form various toxic by-products during the investigated process [3]. Higher light intensity generally increases the rate of photocatalytic reactions by generating more electron-hole pairs. However, there is a saturation point beyond which additional intensity does not significantly enhance the degradation rate [28,35]. Recent advancements in process intensification strategies, including hybrid systems and innovative photoreactor designs, have significantly improved photocatalytic efficiency. These approaches could highlight the potential for overcoming mass and photon transfer limitations, which might be crucial for the degradation of PAHs [36].

Despite the progress in utilizing ZnO-based and other similar nanocomposites for environmental remediation, challenges remain in terms of scalability, long-term stability, and ecological safety of the nanomaterials themselves. The ongoing research aims to tackle these issues by developing more sustainable photocatalytic systems that can operate efficiently under real environmental conditions [21,22,37,38].

This paper will provide in-depth information on the current state of research on the photocatalytic degradation of anthracene and phenanthrene using ZnO-based and similar nanocomposites.

2. Photocatalytic Degradation of Anthracene

In a study by Hassan et al. (2015) [39], the kinetics and mechanisms involved in the photocatalytic degradation of anthracene using ZnO nanoparticles were thoroughly examined. The research demonstrated that decreasing the initial anthracene concentration while increasing the photocatalyst dose enhanced the degradation efficiency. The optimal conditions included maintaining the solution at pH = 7, with a 240-min irradiation period and a catalyst concentration of 1000 μg/L. Under these conditions, the degradation efficiency of anthracene reached approximately 96%. After 6 h of irradiation, intermediates were isolated using chloroform extraction and analyzed through GC-MS. The primary

degradation product identified was 9,10-anthraquinone, regarded as considerably less toxic, along with small amounts of phthalic acid (confirmed by both gas chromatography and high-performance liquid chromatography).

It was shown that 9,10-anthraquinone exhibits significantly lower toxicity compared to anthracene. In toxicity studies, the acute oral LD_{50} (lethal dose for 50% of the exposed population) for anthraquinone in rats exceeds 5000 mg/kg, while the acute dermal LD_{50} in rabbits is also above 5000 mg/kg. Furthermore, anthraquinone is non-toxic to various aquatic species, including carp, trout, and *Daphnia magna*. In contrast, anthracene shows considerable toxicity, with an LD_{50} of 430 mg/kg in mice and a dermal LD_{50} of over 1320 mg/kg in rats. Additionally, anthracene poses significant risks to fish, with an LC_{50} of 0.001 mg/L for bluegill sunfish over 96 h and an EC_{50} of 0.1 µg/L for *Daphnia magna* over 48 h. The ecotoxicity data for phthalic acid indicate an acute LC_{50} for fish (48 h) greater than 1,000,000 µg/L, as reported in the ECOTOX database [39].

The study by Theurich et al. (1997) [40] focused on understanding the photocatalytic degradation pathways of naphthalene and anthracene when exposed to UV-irradiated TiO_2 nanoparticles. Gas chromatography-mass spectrometry (GC-MS) was employed to identify the degradation products formed during the photocatalytic process, and a detailed reaction mechanism was proposed to explain the formation of detected intermediates. The researchers proposed a comprehensive reaction mechanism and the formation of various intermediates. In the case of anthracene, the study identified phthalic acid and 9,10-anthraquinone as the primary stable intermediates during its photocatalytic degradation. Figures 1 and 2 depict the proposed degradation pathways of anthracene, highlighting the role of hydroxyl radicals ($^{\bullet}OH$), which are potent oxidants, in these processes.

The investigated photocatalytic degradation occurs in the following way: (1) hydroxyl radicals attack position 9 of the anthracene molecule, and (2) oxidation at position 10. This sequence forms a hydroperoxy radical, which can further degrade through the two distinct pathways. One of the pathways involves the removal of a hydrogen atom, leading to water loss and further oxidation by hydroxyl radicals, forming a semiquinone radical that is subsequently oxidized to anthraquinone. Alternatively, the elimination of $HO_2^{\bullet}$ produces anthranol, an unstable tautomeric enol form of anthrone, which can be oxidized through an unstable anthrone peroxide to anthraquinone. Notably, while anthrone itself was not identified during the direct oxidation of anthracene, its small amounts were detected when anthraquinone was used as a model compound, suggesting possible reversibility or reduction of anthraquinone to anthrone. After 18 h of UV irradiation, significant amounts of phthalic acid, 1-hydroxy-9,10-anthraquinone, and 1,4-dihydroxy-9,10-anthraquinone were identified, along with trace amounts of 1,2-dihydroxy-9,10-anthraquinone and anthrone, as shown in Figure 2.

It is proposed that 9,10-anthraquinone can be further attacked by hydroxyl radicals at the preferred position 1, ultimately leading to the formation of 1-hydroxy-9,10-anthraquinone, and subsequently to 1,2-dihydroxy-9,10-anthraquinone and 1,4-dihydroxy-9,10-anthraquinone through additional hydroxyl radical attacks. While the presence of tri- and multi-hydroxy-9,10-anthraquinones has not been confirmed, it is expected that these dihydroxy-9,10-anthraquinones will undergo further oxidation, leading to the destabilization of the hydroxylated benzene ring, followed by ring cleavage and formation of phthalic acid. Additionally, the formation of an endoperoxide, an intermediate during the direct photocatalytic degradation of anthracene in the presence of oxygen, was not detected. The formation of trace amounts of anthrone can be explained by a side reaction starting from 9,10-anthraquinone, where electrons are directly transferred from TiO_2 to the quinone, followed by acid-catalyzed water elimination. Anthrone itself will be reoxidized back to 9,10-anthraquinone. It is suggested that ring cleavage in 9,10-anthraquinone does

not occur at the 9,10-positions, as none of the expected intermediates (except for phthalic acid), such as salicylic acid for symmetric cleavage and catechol for asymmetric cleavage, were detected. Instead, the researchers propose further oxidation of 9,10-anthraquinone by hydroxyl radicals [40].

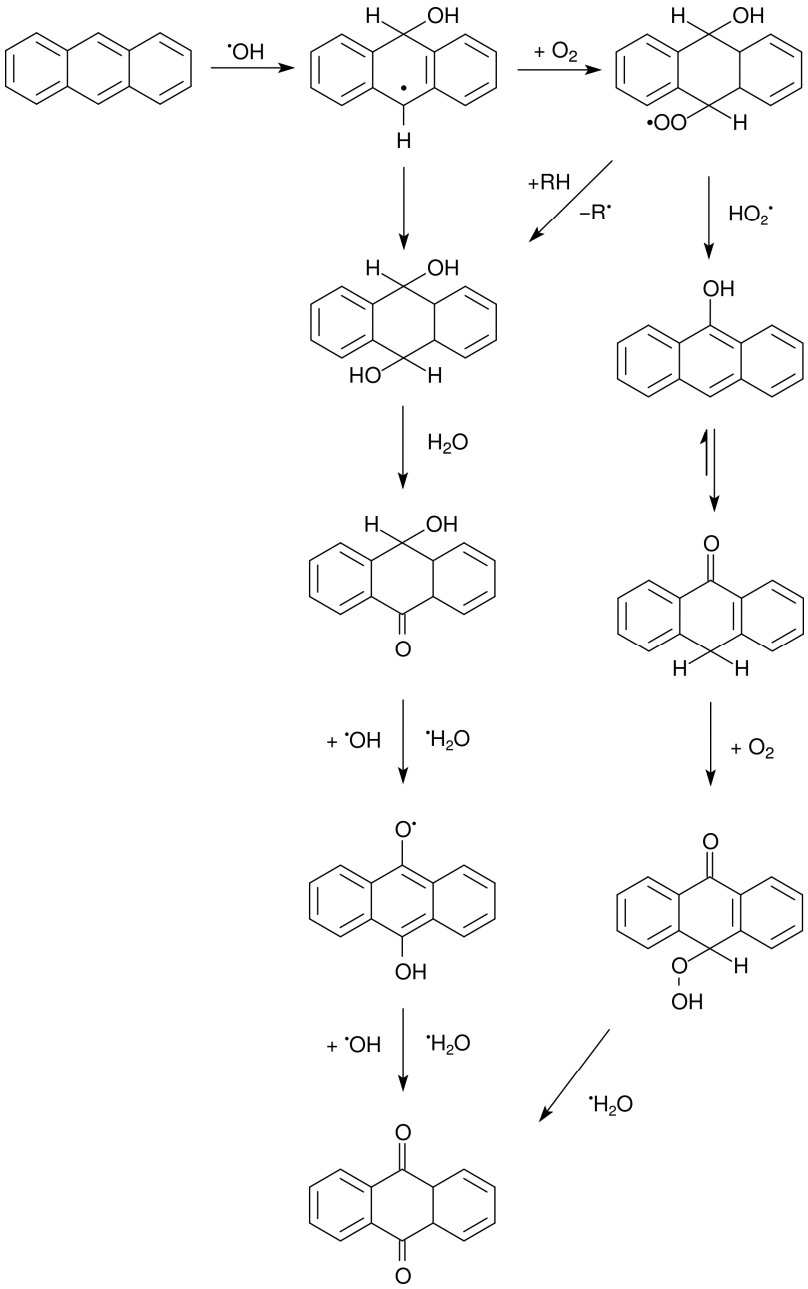


Figure 1. Mechanism of anthracene degradation to 9,10-anthraquinone.

Nguyen et al. (2020) [41] discuss two primary pathways for the photodegradation of anthracene. The first pathway identifies 9,10-anthraquinone as the main degradation product. This has been supported by several studies utilizing different nanocomposites such as n-ZnO/p-MnO, GaN, and ZnO nanoparticles. Hydroxyl radicals are generated on the surface of photocatalysts under UV or visible light. These radicals can attack anthracene at the 9 and 10 positions, leading to the formation of 9,10-anthraquinone, as depicted in Figure 3.

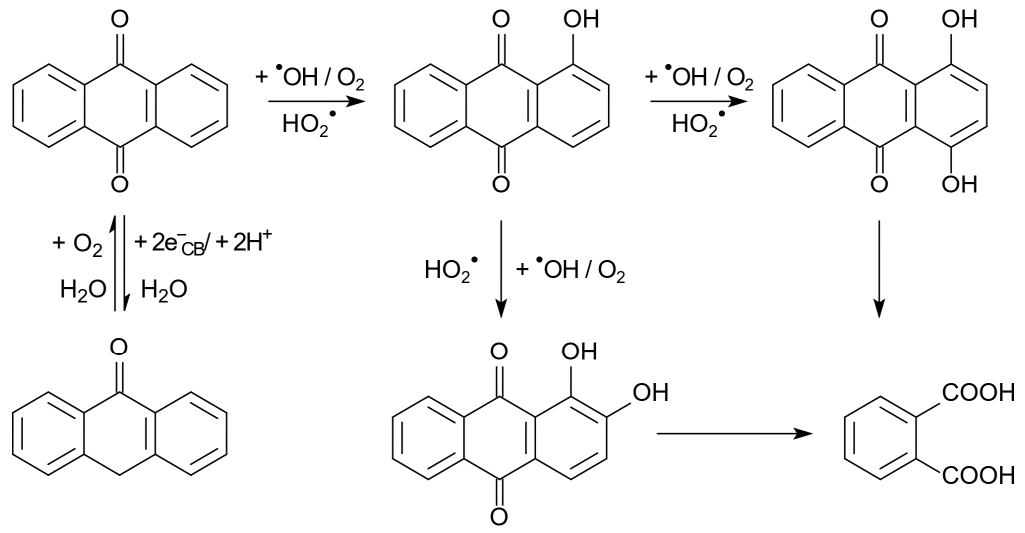


Figure 2. Mechanism of 9,10-anthraquinone degradation to phthalic acid.

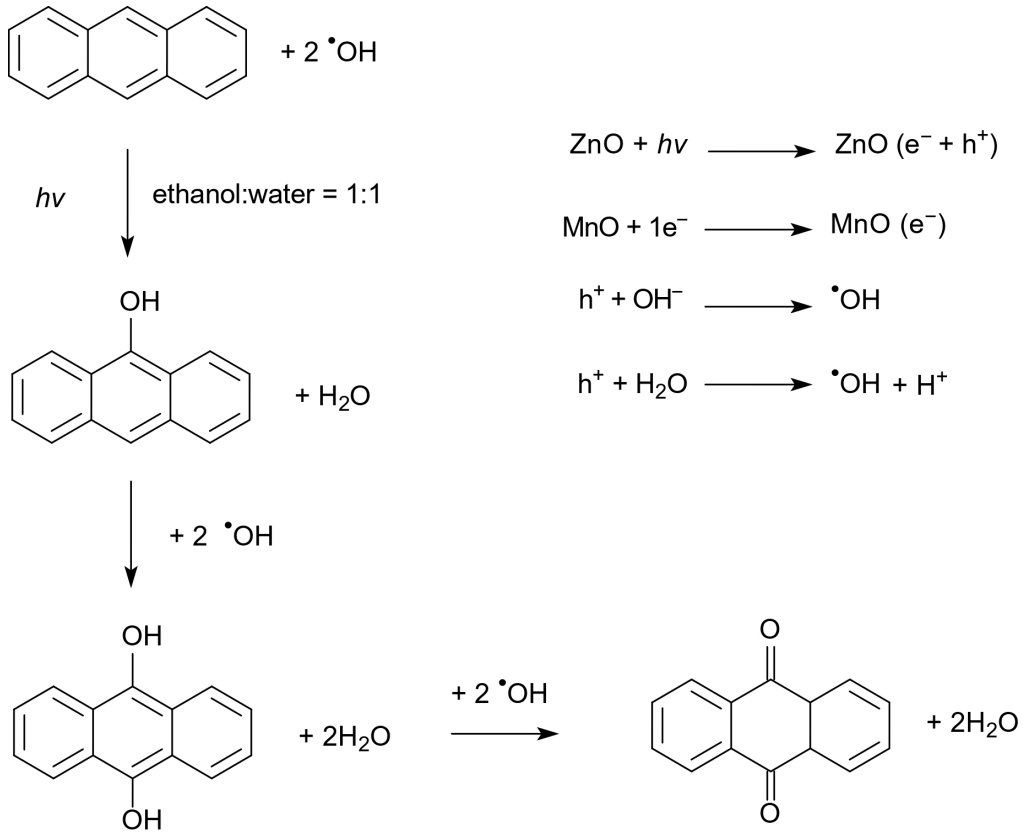


Figure 3. Proposed mechanism for anthracene degradation in the presence of n-ZnO/p-MnO nanocomposites.

According to Nguyen et al. (2020) [41], the second proposed pathway for the photodegradation of anthracene involves its reaction with hydroxyl radicals to form 3-hydroxy-2-naphthoic acid (1, ion mass-to-charge ratio—m/z = 191), which is presented in Figure 4. This intermediate can further degrade into several products, including benzene (3, m/z = 78), malealdehyde (4, m/z = 83), naphthalene (2, m/z = 128), and 4-oxobut-2-enoic acid (5, m/z = 101).

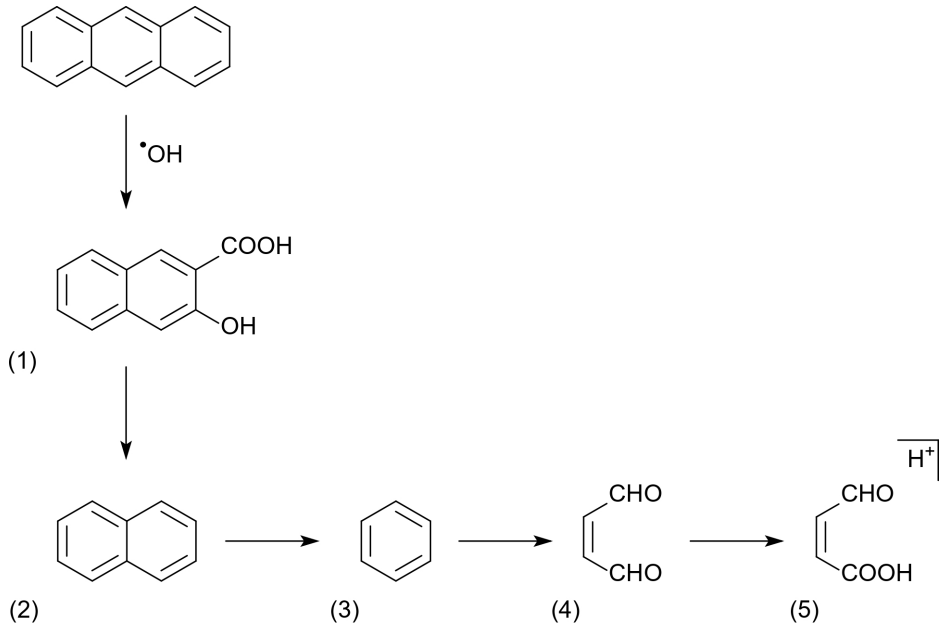


Figure 4. Proposed mechanism for anthracene degradation in the presence of potassium-zinc-hexacyanoferrate (KZnHCF) nanoparticles.

Chen et al. (2015) [42] investigated the use of Cu-ZnO heterostructures for the photocatalytic degradation of anthracene, highlighting the role of copper nanowires (Cu NWs) in enhancing the separation efficiency of photoinduced e^- and h^+. This separation significantly reduces the recombination rate of charge carriers, promoting more effective photocatalysis. Under UV irradiation, photoelectrons are swiftly transferred from the ZnO surface to the Cu NWs, leaving numerous holes on the ZnO surface. The unique brush-like heterostructures increase the specific surface area and provide more active sites, enhancing light absorption and facilitating the diffusion and adsorption of anthracene molecules. The primary rate-determining step involves the diffusion of hydroxyl radicals from the methanol solvent, leading to the isomerization of anthranol to anthrone. Subsequently, hydroxyl radicals attack anthrone, forming 9,10-dihydroxy-anthracene, which is then oxidized to anthraquinone on the Cu-ZnO surface. High-performance liquid chromatography (HPLC) analysis confirmed that the reaction mixture consisted of approximately 90% anthraquinone and 10% anthracene, closely matching the spectrum of the standard solution. Thus, Cu-ZnO nanomaterials are effective in degrading anthracene into anthraquinone.

The Cu-ZnO nanomaterial showed the highest efficiency in degrading anthracene, outperforming its effectiveness on naphthalene and phenanthrene. This superior performance is attributed to the interaction between benzene rings, which enhances UV light sensitivity and electron transport. Additionally, isomerization can modify the hybrid/resonant orbital structure, affecting UV light response. The presence of more benzene rings increases delocalization of the π-electron cloud, resulting in molecular instability. According to molecular orbital theory, the energy level of the highest occupied molecular orbital (HOMO) indicates the molecule's electron-donating ability, while the lowest unoccupied molecular orbital (LUMO) reflects its electron-accepting capability [42]. The energy difference (△E) between HOMO and LUMO correlates with molecular stability, with a larger △E signifying greater stability. Density functional theory (DFT) calculations show that naphthalene has a higher △E value than phenanthrene and anthracene, indicating greater stability. Consequently, phenanthrene and anthracene, with their additional benzene rings and more delocalized π-electrons, are more easily activated under UV light, whereas naphthalene, with fewer delocalized π-electrons, is less reactive. Therefore, when catalyzed by Cu-ZnO nanomaterials, naphthalene has fewer activated π-electrons available for attack by h^+, generated in ZnO

nanoparticles, making it less susceptible to photodegradation compared to phenanthrene and anthracene.

Rani et al. (2019) [43] evaluated the photocatalytic degradation of anthracene using several bimetallic nanocomposites, including NiO-ZnO, $ZnCo_2O_4$, $MnCo_2O_4$, and $CoFe_2O_4$. Their findings revealed that NiO-ZnO was the most effective. Transmission electron microscopy confirmed that the NiO-ZnO, $ZnCo_2O_4$, and $CoFe_2O_4$ nanospheres, as well as $MnCo_2O_4$ nanoplates, had particle sizes ranging from 10 to 30 nm. They proposed a degradation mechanism, depicted in Figure 5, where anthracene degradation begins with hydroxyl radicals attacking positions 9 and 10, forming non-toxic diols or quinones.

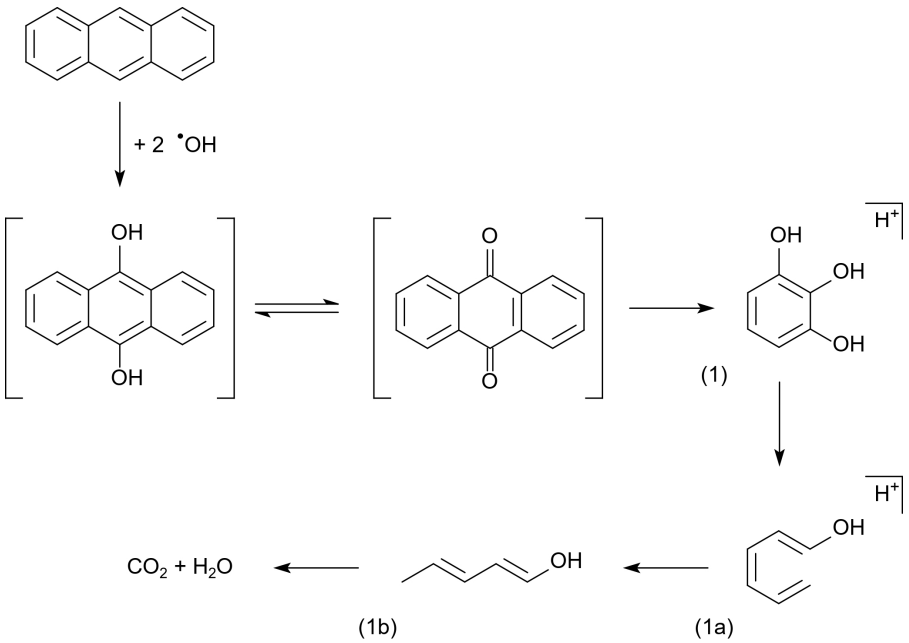


Figure 5. Mechanism of anthracene degradation on ZnO-NiO nanocomposite.

GC-MS analysis identified 1,2,3-benzotriol (1, m/z = 128), suggesting its formation through ring opening and hydroxylation of anthracene-9,10-diol. Further oxidation and ring opening of this intermediate produce simpler products such as (1*E*, 3*Z*)-hexa-1,3,5-trien-1-ol (1a, m/z = 98) and (1*E*, 3*E*)-penta-1,3-dien-1-ol (1b, m/z = 85), which are expected to undergo mineralization. The study highlights that the photodegradation of anthracene using ZnO under UV light to form 9,10-anthraquinone emphasizes the superior efficacy of bimetallic nanocomposites over single metal oxides [43].

Sliem et al. (2019) [44] investigated the intermediates formed during the photocatalytic degradation of anthracene using ZnO nanoparticles. The intermediates were extracted with chloroform and identified via GC-MS analysis. After 4 h of reaction, the analysis revealed a series of peaks with retention times (Rt) between 5 and 55 min. Specifically, the decomposition of anthracene resulted in two primary products: ethyl 4-formylbenzoate detected at an Rt of 36.78 min, and isopropyl methyl ester of 1,2-benzenedicarboxylic acid at a Rt of 31.59 min. These peaks corresponded to 98.23% and 0.85% of the respective compounds. The study demonstrated that regardless of the solvent mixture (ethanol and water or acetone and water), ZnO nanoparticles facilitated the consistent photocatalytic degradation of anthracene, producing various intermediates. This aligns with the predicted reactive sites on anthracene, where positions 9 and 10 are preferentially attacked [44]. The presence of acetone significantly influences the degradation pathways of PAHs. For instance, Woo et al. (2009) [45] state that when it comes to solvent mixtures, increasing concentrations from 1% to 16% can lead to higher concentrations and a wider variety of

intermediates, thus allowing for a more complete degradation pathway. This addition helps in improving the solubility of PAHs, facilitating their contact with the photocatalyst. In the work of Sliem et al. (2019) [44], there were no signals indicating the presence of ethanol or its oxidation products.

Martínez-Vargas et al. (2019) [46] synthesized nanocomposites with varying manganese content, achieving the best results with an Mn concentration of 2.25%. The experimental setup included a 20 ppm anthracene solution, a catalyst loading of 1.5 mg ZnO/MnO, UV irradiation, a pH of 12, room temperature, and a reaction time of 40 min. Researchers have highlighted that the n-ZnO/p-MnO nanocomposite with 2.25% Mn demonstrated superior degradation performance compared to other formulations. Although the exact degradation percentage was not specified, this formulation exhibited the highest photocatalytic efficiency among those tested. This enhanced performance is attributed to improved charge separation and transfer at the semiconductor junction, thereby reducing recombination rates and facilitating the formation of reactive species such as hydroxyl radicals, which effectively degrade anthracene into CO_2, H_2O, and other inorganic compounds. This work underscores the potential of n-ZnO/p-MnO nanocomposites in environmental remediation applications.

Similarly, the study conducted by Kou et al. (2010) [47] explored the photocatalytic degradation of polycyclic aromatic hydrocarbons (PAHs) using GaN solid solutions, both unmodified and modified with platinum. The research demonstrated that these solid solutions exhibit excellent activity for degrading PAHs such as phenanthrene, anthracene, acenaphthene, and benz[a]anthracene. Notably, the activity of the GaN catalyst was significantly enhanced by platinum modification, potentially enabling complete degradation of these PAHs under visible light within varying but specific time frames—phenanthrene and benz[a]anthracene within an hour and three hours, respectively, indicating the effectiveness of this catalyst under practical environmental conditions. The mechanism highlighted involves the interaction of generated holes and active hydrogen species with the PAH molecules, forming active intermediates that react with oxygen and further active species to produce less harmful or simple inorganic molecules such as CO_2 and H_2O.

In a recent study on the photocatalytic breakdown of anthracene with Cu-doped ZnO nanocomposites, a remarkable 94% efficiency was achieved under conditions that mimic natural environment exposure using sunlight and a neutral pH. This study revealed that the degradation process adheres to first-order kinetics, beginning primarily with the adsorption of anthracene onto the catalyst's surface, which suggests a critical role for surface adsorption in the overall degradation pathway. The inclusion of copper in the ZnO matrix significantly bolsters the photocatalytic activity. This enhancement is primarily due to improved electron-hole separation and charge transfer within the semiconductor junction, which effectively minimizes recombination losses. Such findings underscore the potential of using natural sunlight as a sustainable and energy-efficient light source for the photocatalytic degradation of hazardous organic compounds in real-world applications. Furthermore, the Cu@ZnO nanocomposite displayed notable durability and reusability, maintaining high degradation efficiency across multiple cycles. This reusability highlights the nanocomposite's cost-effectiveness and practical utility for ongoing environmental cleanup efforts. The study thus positioned Cu-doped ZnO nanocomposites as promising candidates for the remediation of water systems contaminated with polycyclic aromatic hydrocarbons like anthracene [6].

The results presented in Table 1 demonstrate the efficiency of anthracene's photocatalytic degradation under various reaction conditions.

Table 1. The photocatalytic degradation efficiency of anthracene using various nanocatalysts.

PAH Compound	Nanocatalyst	Photocatalysis Conditions	Degradation Efficiency	Reference
Anthracene	ZnO NPs (green synthesized using corriandrum sativum leaf extract)	25 µg/L anthracene; 1000 µg/L ZnO; UV; pH = 7; 25 °C; 240 min	96%	[39]
	ZnO NPs (chemically synthesised)	100 µg/L anthracene; 1000 µg/L ZnO; UV; pH = 7; 25 °C; 240 min	31%	
	Cu@ZnO nanobrushes	50 µg/L anthracene; 10 mg Cu@ZnO; UV; room temperature; >160 min (graph value)	90%	[42]
	n-ZnO/p-MnO (Mn = 2.25%)	20 ppm anthracene; 1.5 mg ZnO/MnO; UV; pH = 12; room temperature; 40 min	Best degradation performance, exact percentage not provided	[46]
	GaN:ZnO	3 mg of PAH dissolved in the mixture of 30 mL of water and 30 mL of acetone; 3 mg Pt–GaN:ZnO; 300 W Xenon lamp with cut-off filter > 420 nm; pH = 7; room temperature; 6 h	25% (not explicitly stated)	[47]
	Pt–GaN:ZnO		100% (not explicitly stated)	
	KZnHCF nanocubes	50 mg/L anthracene; 25 mg KZnHCF; sunlight; pH = 7; room temperature; 48 h	93%	[5]
	Cu@ZnO	10 mg/L anthracene; 10 mg Cu@ZnO; pH = 7; 120 min; natural sunlight	94%	[6]
	ZnO NPs	23 mg/L anthracene; 55.6 mg/L ZnO; UV light (40 W, 220 V, 1 mW/cm^2); pH 7.2; 25 °C; 280 min	33.14%	[44]
	ZnO NPs + H_2O_2	23 mg/L anthracene; 55.6 mg/L ZnO + 300 µL H_2O_2 (30%); UV light (40 W, 220 V, 1 mW/cm^2); pH 7.2; 25 °C; 50 min	84.02%	

3. Photocatalytic Degradation of Phenanthrene

Zhao et al. (2016) [48] developed a novel photocatalyst using TiO_2 as a precursor, employing a two-step process involving hydrothermal reaction at 150 °C followed by calcination at 600 °C. The resultant Co-TNTs-600 nanomaterial demonstrated high photocatalytic efficiency for the degradation of phenanthrene under sunlight, achieving a removal rate of 98.6% within 12 h at a dosage of 1 g/L of Co-TNTs-600. The proposed mechanism for the photocatalytic degradation of phenanthrene using Co-TNTs-600 is depicted in Figure 6.

It was observed that after 60 min of photocatalytic degradation of phenanthrene using Co-TNTs-600, two primary intermediates were formed: (1,1-biphenyl)-2,2-dicarboxaldehyde and 9,10-phenanthrenequinone. The formation of 9,10-phenanthrenequinone occurs through the ketonization of the hydroxylated benzene ring of phenanthrene (steps 1–2–3 in Figure 6), while (1,1-biphenyl)-2,2-dicarboxaldehyde results from the ring-opening of 9,10-phenanthrenequinone (Step 4). Additionally, the formation of 3,4-benzocoumarin takes place in the mechanism, before the subsequent ring opening (Steps 5–7). After 3 h, 9,10-phenanthrenequinone was no longer detected, and a new intermediate, bis(2-ethylhexyl) phthalate, appeared, indicating further benzene ring opening and subsequent alkylation by photo-activated alkanes ($^{\bullet}$R) (Steps 6/7–8). After 6 h, bis(2-ethylhexyl) phthalate also disappeared, with 93% of the initial phenanthrene and 27% of (1,1-biphenyl)-2,2-dicarboxaldehyde being degraded. The subsequent oxidation of phthalates led to the formation of simpler organic compounds such as cyclohexanols, alkanoic acids, alkenes, alkanes, and alcohols (Step 9), which were eventually mineralized into CO_2 and H_2O (Step 10). The study suggests that the photodegradation pathway of phenanthrene in the presence of Co-TNTs-600 nanocomposites is consistent with those observed for other photocatalysts, with key intermediates like (1,1-biphenyl)-2,2-dicarboxaldehyde and 9,10-phenanthrenequinone expected to undergo mineralization. Thus, Co-TNTs-600 is an effective photocatalyst for the degradation of persistent PAHs under sunlight.

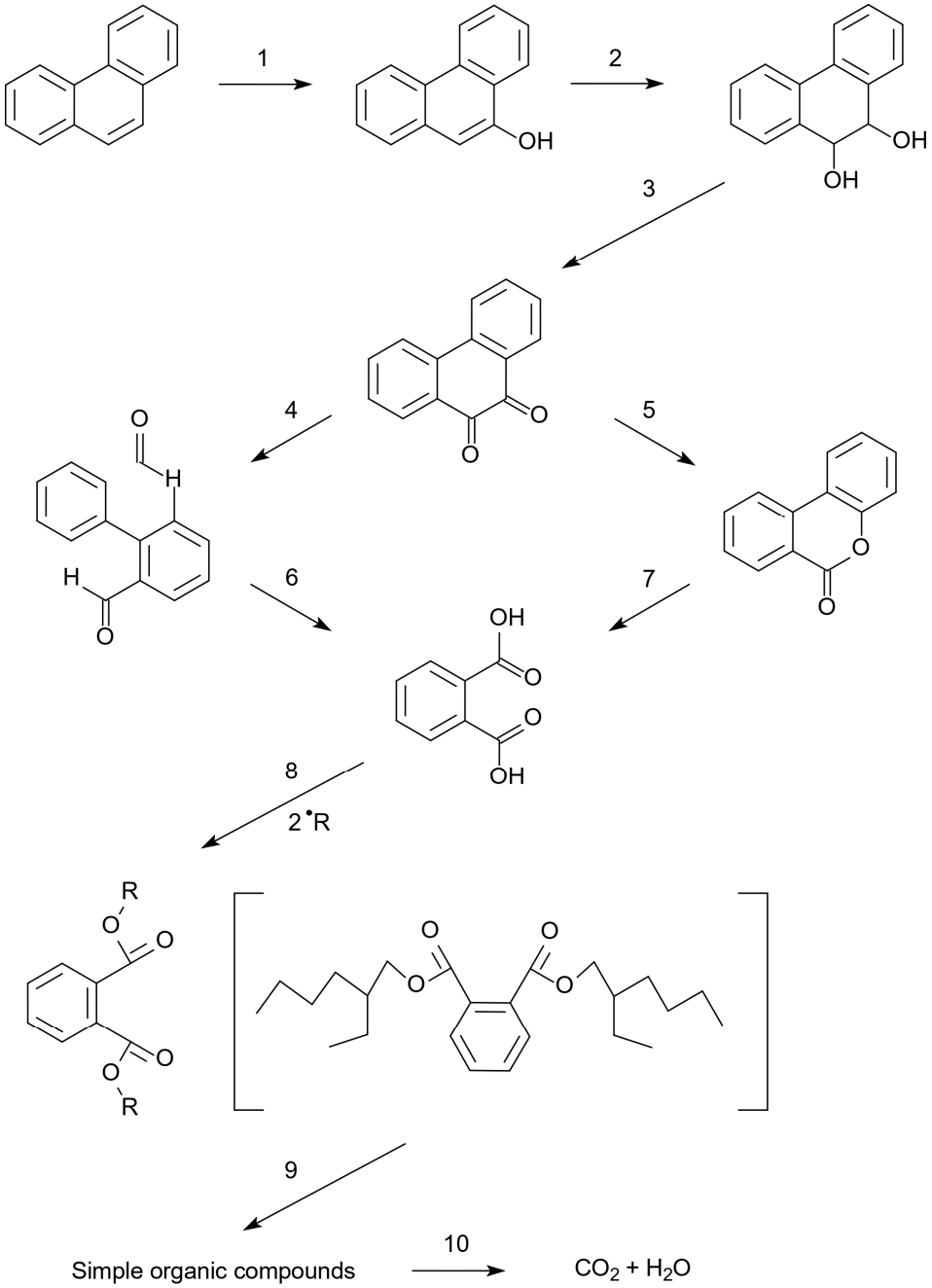


Figure 6. Proposed mechanism for the degradation of phenanthrene in the presence of Co-TNTs-600.

Rani et al. (2019) [43] evaluated the photocatalytic degradation of phenanthrene using bimetallic nanocomposites such as NiO-ZnO, $ZnCo_2O_4$, $MnCo_2O_4$, and $CoFe_2O_4$. Their results showed that NiO-ZnO was the most efficient catalyst, similar to their findings in anthracene degradation experiments. The researchers proposed a degradation mechanism, as illustrated in Figure 7.

Because of the relative stability of phenanthrene, its photo-oxidation proceeds more slowly and results in higher molecular weight intermediates. GC-MS analysis identified the presence of 3-hydroxy-2-naphthoic acid (1, m/z = 191), which likely forms through hydroxylation of the sterically hindered ring of the intermediate phenanthrene-9-ol, followed by ring cleavage via oxidation. Further ring opening and hydroxylation of 3-hydroxy-2-naphthoic acid leads to the formation of 1,2,4-benzenetriol (1a, m/z = 128). This compound is subsequently oxidized into simpler intermediates such as (*Z*)-3-hydroxyacrylic acid (1b; m/z = 91) and (*Z*)-4-oxobut-2-enoic acid (1c; m/z = 101), which are then mineralized

through the action of numerous hydroxyl radicals. At neutral pH, the nanocomposites demonstrated excellent capability in degrading 2 mg/L of the tested PAH (Anthracene: 98%; Phenanthrene: 93%) within 12 h of sunlight exposure [43].

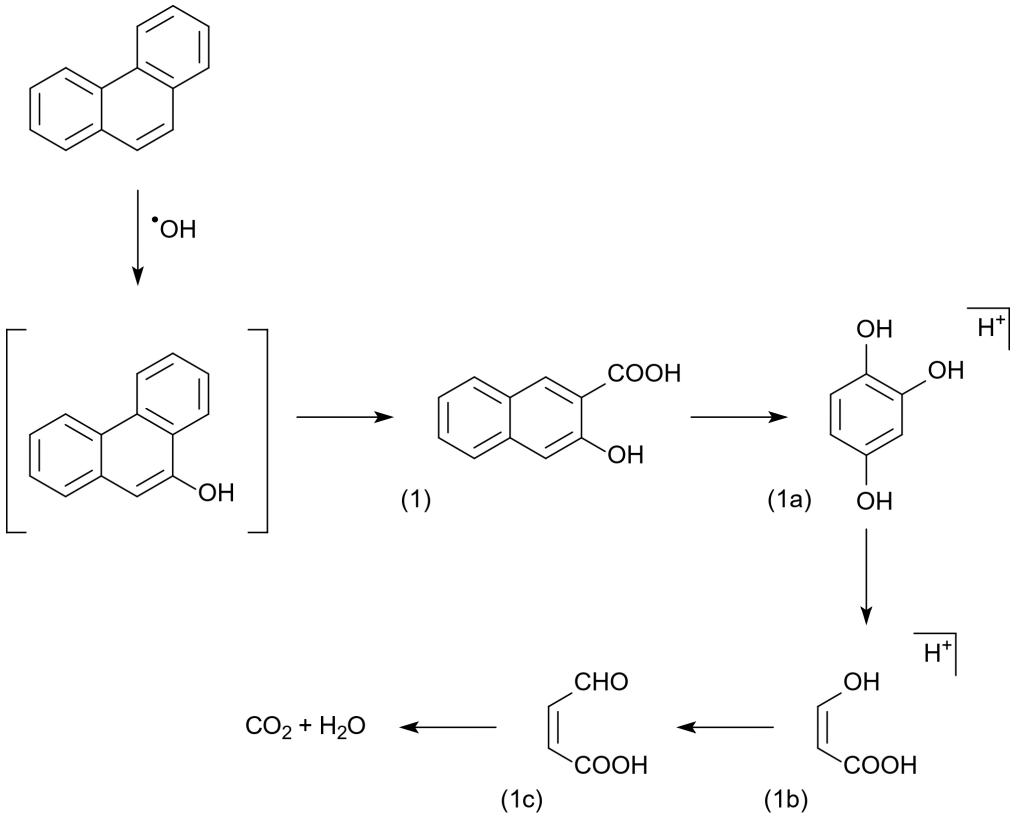


Figure 7. Mechanism of phenanthrene degradation on ZnO-NiO nanocomposite.

Significantly higher efficiency of PAH degradation under sunlight (anthracene: 98% and phenanthrene: 93%) compared to dark conditions (40–50%) verified the photocatalytic activity of the nanocomposites. In the absence of sunlight, these nanocomposites primarily adsorbed PAHs onto their surfaces due to their large specific surface area and negative zeta potentials. When exposed to sunlight, the photoactive catalyst experiences electronic excitation, generating electron-hole pairs and subsequent hydroxyl radicals in the presence of water and oxygen. The presence of two metal oxides with different band gaps enables the generated charge carriers to remain in the conduction bands for extended periods. This prolonged generation of hydroxyl radicals significantly enhances degradation efficiency. It is estimated that around 30% of the residual carbon content detected by GC-MS analysis after the photocatalytic degradation of the tested PAHs is from smaller intermediates [43].

Chauhan et al. (2021) [49] explored the role of h^+ and reactive oxygen species (ROS), such as hydroxyl and other radicals, in the degradation of phenanthrene by using various scavengers to elucidate the photocatalytic mechanisms. Ammonium oxalate was employed as a h^+ scavenger to test the involvement of photo-generated h^+ in the photocatalytic reactions. Isopropanol served as a hydroxyl radical scavenger, chosen for its high reaction rate constant with oxidants and its relatively low reactivity with reductants. Sodium azide was used to trap reactive oxygen species, particularly singlet oxygen ($^1O_2$) and hydroxyl radicals ($^\bullet$OH). Additionally, 1,4-benzoquinone was utilized to detect and capture superoxide anions ($^\bullet O_2$). This reactive oxygen species analysis identified four intermediates from phenanthrene after 30 min of irradiation: (1,1-biphenyl)-2,2-dicarboxaldehyde (5), 9,10-phenanthrenequinone (4), phenanthro [9,10-b]oxirane (3), and 9-phenanthrol (2). The intermediates formed during the photocatalytic degradation of phenanthrene primarily

target positions 9 and/or 10, which are the most reactive sites in its aromatic structure. This targeting is predominantly mediated by $^{\bullet}O_2$ species. Other than 9,10-phenanthrenequinone, the identified complexes disappeared after two hours of irradiation, suggesting that these intermediates undergo multiple short-lived photocatalytic transformations compared to the phenanthrene molecule itself.

Bai et al. (2017) [50] examined the reaction involving hydroxyl radicals attacking electron-rich conjugated sites, which resulted in the formation of hydroxylated phenanthrene. This reaction led to the production of lactones and diketones, which are precursors for ring-opening configurations in photocatalysis. As the degradation process continued, these ring-forming compounds transformed into phthalates and their derivatives, which are common intermediates in the degradation of PAHs. Eventually, these phthalates were converted into acyclic hydrocarbons or alcohols through polymerization and ultimately mineralized into water and carbon dioxide. Table 1 summarizes the potential intermediates in the degradation of phenanthrene based on the type of photocatalytically active material used.

Chauhan et al. (2021) [49] highlighted that the introduction of different nanomaterials, such as graphene oxide (GO), can significantly enhance the photocatalytic efficiency by improving charge separation and reducing recombination rates of photo-generated electron-hole pairs. For example, GO/ZnO nanocomposites demonstrate a higher photocatalytic activity compared to pristine ZnO, leading to a more efficient degradation process. These researchers provided a comprehensive overview of the various degradation intermediates formed during the photocatalytic degradation of phenanthrene using different catalysts, as shown in Table 2.

Table 2. Overview of the potential intermediates based on the type of photocatalytically active material and type of reactive species during phenanthrene degradation [49].

Catalyst	Reactive Species	Intermediates
TiO_2-ZnHCF	$^{\bullet}OH$	9-Hydroxyanthracene; 2,2′ Diphenic acid; 1,2,3-Trihydroxybenzene; 2,3-Dihydroxybenzoic acid; Glycolaldehyde
Graphite oxide-TiO_2-$Sr(OH)_2/SrCO_3$	$^{\bullet}OH$ and $O_2^{\bullet-}$	9-Hydroxyanthracene; Phenanthro [9,10-*b*]oxirene; 9,10-Phenanthrenedione; 2-Cyclohexen-1-one; 1,2-Cyclohexanedione; Octyl acrylate
		(1,1′-Biphenyl)-2,2′-dicarboxyaldehyde; Phtalates; 2-Cyclohexen-1-ol; 2-Hexenal; 5-Hydroxymethyldihydrofuran-2-one
GO/Ag_3PO_4	$^{\bullet}OH$, h^+ and O_2^-	(1,1′-Biphenyl)-2,2′-dicarboxyaldehyde; 1,2-benzenetricarboxylic acid; trimethyl ester
NiO-ZnO	$^{\bullet}OH$	9-Phenanthrenol; 3-hydroxy-2-naphthoic acid; benzene-1,2,4-triol; (1*E*, 3*Z*)-
		hexa-1,3,5-trien-1-ol; (1*E*, 3*E*)-penta-1,3-dien-
		1-ol
TiO_2	$^{\bullet}OH$ and h^+	9-Hydroxyphenanthrene; 9,10-Dihydroxyphenanthrene; 9,10-Phenanthrenediol
		9-Fluorenone; 6H-benzo[c]chromen-6-one
KZnHCF	$^{\bullet}OH$	Naphthalene-1,2,6,7-tetraol; Naphthalene; (*Z*)-3-Hydroxyacrylic acid; (*Z*)-4-Oxobut-2-enoic acid

The degradation of phenanthrene through photocatalysis involves various intermediates depending on the catalyst used. The catalysts listed in Table 2 include different metal-based nanocomposites and their corresponding active species, which play a significant role in the degradation mechanism. The primary active species involved in these processes are hydroxyl radicals ($^{\bullet}OH$), superoxide radicals ($^{\bullet}O_2^-$), and photo-generated holes (h^+). The presence of different active species also affects the nature and stability of the intermediates formed. For example, the formation of 9,10-phenanthrenedione and (1,1′-biphenyl)-2,2′-dicarboxaldehyde as intermediates indicates that the oxidative attack primarily occurs at positions 9 and 10 of the phenanthrene molecule [49]. These intermediates are further transformed into less toxic compounds, eventually mineralizing into CO_2 and H_2O under optimal conditions.

Kou et al. (2010) [47] explored the degradation efficiency of phenanthrene, anthracene, acenaphthene, and benz[a]anthracene under visible light using GaN and Pt-GaN nanocomposites. While the conversion rates of phenanthrene varied between GaN and Pt-GaN, the intermediates formed were quite similar. The main intermediates were identified as compounds biphenyl-2,2′-dicarbaldehyde (4) and phenanthrene-9,10-dione, which form through the oxidation at positions 9 and 10 of phenanthrene. Additionally, two isomers with a molecular ion of 212 were detected during photodegradation. Based on standard spectra, a peak was identified as 9,10-dihydro-9,10-dihydroxyphenanthrene, and an additional peak was tentatively identified as 1,4-dihydro-1,4-dihydroxyphenanthrene based on mass spectrum fragmentation patterns. These intermediates, being hydrogenated-oxidation products, suggest that the oxidation process involves hydrogenation. The degradation mechanism proposed is illustrated in Figure 8.

The researchers concluded that PAHs initially undergo hydrogenation and hydroxylation, forming hydroxyl compounds or hydrogenated hydroxyl intermediates. As the reaction time increases, these intermediates are further oxidized into ketones or quinones. Ultimately, through further oxidation, these intermediates are converted into simpler molecules such as CO_2 [47].

Wen et al. (2002) [51] explored the photocatalytic reactions of phenanthrene in aqueous TiO_2 suspensions under UV light, where phenanthrene was pre-adsorbed onto TiO_2 particles. This study showed that phenanthrene could be rapidly and completely mineralized, confirmed by changes in chemical oxygen demand (COD) and spectroscopic analyses of intermediates. It was also observed that pH value, surface coverage, and the amount of TiO_2 have minimal impact on the degradation rate, indicating the high efficiency and robustness of TiO_2 as a photocatalyst in the degradation of phenanthrene.

In the research on the photocatalytic degradation of phenanthrene, Woo et al. (2009) [45] demonstrated how the addition of acetone can significantly affect the degradation pathways and efficiency of phenanthrene decomposition. While acetone increases the solubility of phenanthrene, it also modifies the degradation pathways, leading to the formation of intermediates. These intermediates initially accumulate and are then efficiently broken down, as confirmed by the Microtox® test, which indicated that the photocatalytic process completely detoxifies phenanthrene and its intermediates within 24 h. These findings highlight the importance of optimizing photocatalytic conditions, including solvent concentration and presence, for maximum efficiency in the degradation of PAH compounds.

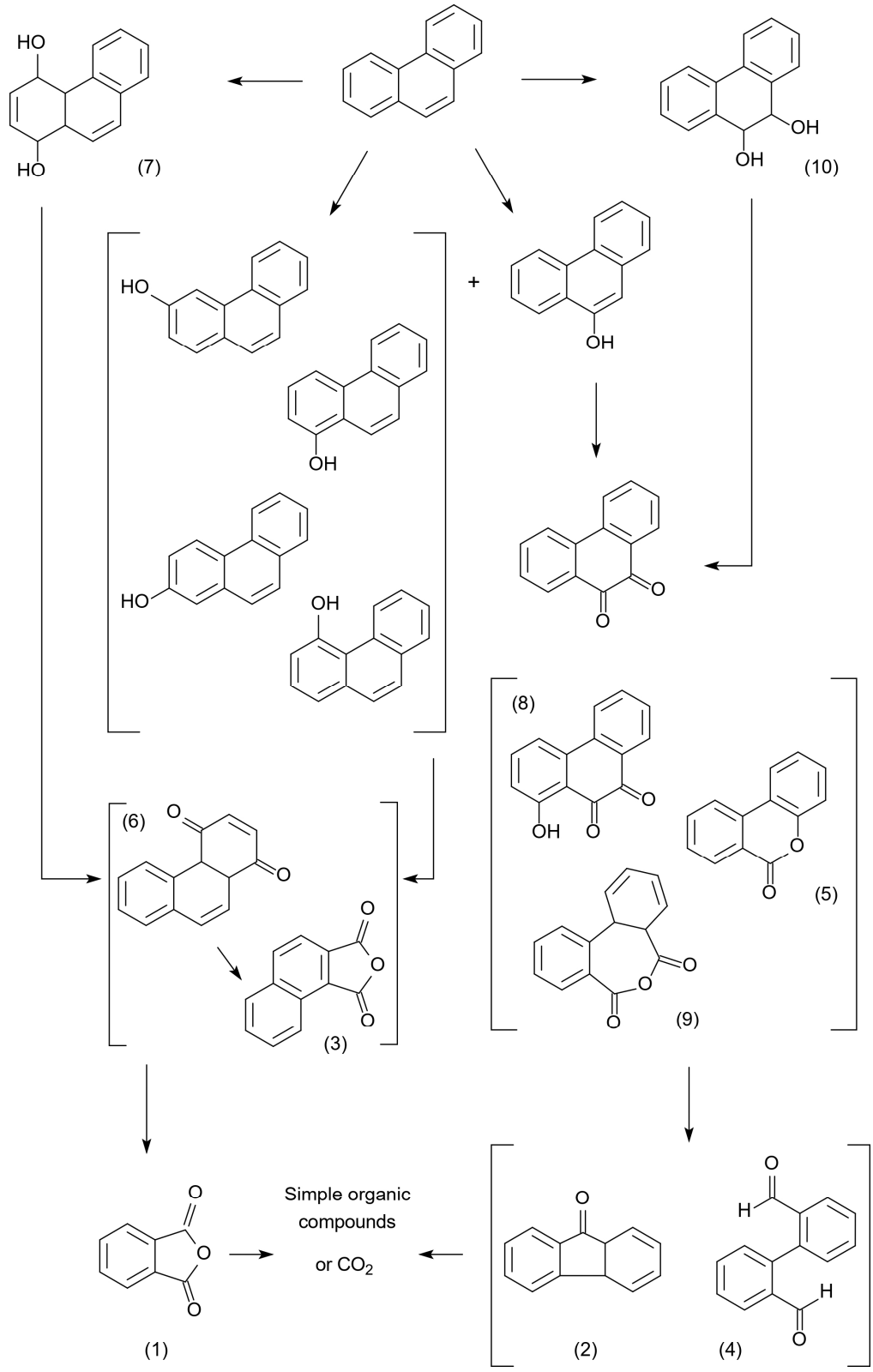


Figure 8. Mechanism of phenanthrene degradation in the presence of GaN:ZnO nanocomposites. The degradation pathway on Figure 8 involves the formation of phthalic anhydride (1), fluorenone (2), 1,2-naphthalenedicarboxylic anhydride (3), biphenyl-2,2′-dicarbaldehyde (4), 6H-dibenzo(b,d)pyran-6-one (5), phenanthrene-1,4-dione (6), phenanthrene-1,4-diol (7), 1-hydroxyphenanthrene-9,10-dione (8), diphenic anhydride (9), phenanthrene-9,10-diol (10), and phenanthrene-9,10-dione.

Zhao et al. (2016) [48] presented a significant advancement in photocatalytic materials when it comes to Co-TNTs, with their ability to enhance the photodegradation rates of

phenanthrene. The Co-TNTs showed a tenfold increase in the degradation rate compared to traditional TiO_2. The cobalt deposition lowered the band gap to 2.8 eV, improving the material's response to visible light and thereby increasing its practical utility under solar radiation. Cobalt oxide within the nanotubes acted as an electron transfer mediator, crucially reducing the recombination of photogenerated electron-hole pairs. The study has also confirmed that Co-TNTs have good reusability and can be separated by gravity, adding to their practical application potential in environmental cleanup efforts.

Rachna et al. (2019) [52] found that the novel TiO_2-based zinc hexacyanoferrate (ZnHCF) nanocomposite, synthesized using a two-step method, demonstrated high photocatalytic degradation of phenanthrene under natural sunlight. The nanocomposite achieved degradation efficiencies of 93–96% in water, 82–86% in soil, and about 81.63–85.43% in river sediment. The nanocomposite exhibited a significant increase in surface area (118.15 m^2/g) and a decrease in band gap energy to 1.65 eV, facilitating superior photocatalytic activity compared to bare materials. The reduced photoluminescence intensity indicated minimized charge carrier recombination. The degradation involved "cation-π" interactions between the nanocomposite and PAH molecules, which are crucial for accelerating the photocatalytic process. The study also identified small by-products of the degradation process, supporting the efficacy of the nanocomposite in breaking down complex organic pollutants.

The results presented in Table 3 demonstrate the efficiency of phenanthrene's photocatalytic degradation under various reaction conditions.

Table 3. The photocatalytic degradation efficiency of phenanthrene using various nanocatalysts.

PAH Compound	Nanocatalyst	Photocatalysis Conditions	Degradation Efficiency	Reference
Phenanthrene	KZnHCF	50 mg/L; 25 mg; Sunlight; pH = 7.0; 25 °C; 48 h	83%	[5]
	Co-TNTs-600	200 µg/L phenanthrene; 1.0 g/L Co-TNTs-600; Solar light; pH = 7.0 ± 0.2; 25 ± 0.2 °C; 12 h	98.60%	[48]
	TiO_2	10 ppm phenanthrene; 0.05g TiO_2; UV; Room temperature; 120 min	80%	[53]
	N-TiO_2	10 ppm phenanthrene; 0.05 g N-TiO_2; UV; Room temperature; 120 min	89%	
	Cu/N-codoped TiO_2	10 ppm phenanthrene; 0.05 g Cu/N-codoped TiO_2; UV; Room temperature; 120 min	94%	
	TiO_2	10 mg/L phenanthrene; 100 mg/L TiO_2; UV light; 24 h	100%	[45]
	TiO_2	50 mg/L phenanthrene; 50 mg TiO_2; UV light (100 W Hg lamp); pH = 5; 25 °C; 2 h	90%	[51]
	TiO_2	2 mg/L phenanthrene; 15 mg TiO_2; Sunlight; pH = 7; 32.3 ± 3.8 °C; 24 h	50%	[52]
	ZnHCF	2 mg/L phenanthrene; 15 mg ZnHCF; Sunlight; pH = 7; 32.3 ± 3.8 °C; 24 h	73%	
	TiO_2@ZnHCF	2 mg/L phenanthrene; 15 mg TiO_2@ZnHCF; Sunlight; pH = 7; 32.3 ± 3.8 °C; 24 h	95%	

4. Critical Assessment of Photocatalytic Materials and Systems

4.1. Comparative Analysis of Metal Oxide Nanomaterials

Among all commonly used nanomaterials, ZnO generally exhibits superior charge mobility (120 cm^2 V^{-1} s^{-1}) and higher quantum efficiency under UV irradiation, while TiO_2 offers greater long-term stability but suffers from rapid charge carrier recombination and limited visible-light utilization. The superior photocatalytic activity of ZnO under UV irradiation can be attributed to its higher exciton binding energy (60 meV) and stronger oxidative potential (+2.7 V vs. SHE). However, the wide bandgap (3.3 eV) and susceptibility to photocorrosion necessitate strategic modifications. Doping with transition metals (Mn, Co, Cd) narrows the bandgap and suppresses electron-hole recombination, while anionic doping (N, C, S) introduces mid-gap states for visible-light absorption. Heterojunction formation creates a type-II band alignment that facilitates charge separation, achieving synergistic effects that outperform individual components. These modifications collectively demonstrate that the performance of ZnO-based photocatalysts is not intrinsic but engineered through bandgap tuning, defect engineering, and interface design to meet specific application requirements [54].

The superior photocatalytic activity of ZnO under UV irradiation, highlighted by Hassan et al. [39] (2015), is experimentally validated through direct comparison with TiO_2. While both semiconductors possess similar band gaps, ZnO exhibits higher quantum efficiency because it absorbs more quanta of light in the UV region. The authors also demonstrate that the performance of ZnO is not solely determined by its intrinsic properties but is profoundly influenced by the synthesis method. Green synthesis using Coriandrum sativum leaf extract produced ZnO nanoparticles with significantly smaller particle sizes (9–18 nm by HR-TEM, 52 nm by DLS) compared to chemically synthesized ZnO (190–210 nm). Furthermore, the green-synthesized ZnO exhibited superior adsorption capacity (60% in the dark) compared to its chemically synthesized counterpart (25%), indicating that the presence of phytochemicals from the plant extract not only controls particle size but also modifies surface properties favorable for pollutant adsorption. Meenu et al. [6] (2024) in their study of synthesized Cu^{2+}-doped ZnO nanocomposites (Cu@ZnO) using Azadirachta indica leaf extract. Comprehensive characterization revealed that Cu doping induced several critical modifications: (i) XRD analysis showed a decrease in crystallite size from 23.9 nm (ZnO) to 21.3 nm (Cu@ZnO), accompanied by increased dislocation density (0.19×10^{-3} to 3.1×10^{-3}), indicating the introduction of structural defects that can serve as electron traps; (ii) BET surface area increased dramatically from 16 m^2/g to 39.2 m^2/g, a 2.5-fold enhancement providing more active sites for pollutant adsorption and reaction; (iii) UV-vis DRS revealed a significant reduction in band gap from 3.4 eV to 2.3 eV, extending light absorption into the visible region; (iv) PL spectroscopy showed lower emission intensity for Cu@ZnO, indicating suppressed electron-hole recombination; (v) zeta potential became more negative (−15.7 mV to −30.2 mV), enhancing colloidal stability and reducing agglomeration. The authors explain the mechanistic role of Cu doping: copper introduces additional energy levels that localize excited electrons from the ZnO conduction band, increasing charge carrier lifetime and shifting light absorption toward the visible region, while the Cu–ZnO interface creates a Schottky-type barrier that reduces charge recombination.

Kou et al. [47] (2010) demonstrated the approach of GaN:ZnO solid solutions synthesis with a wurtzite-type structure and a band gap of 2.6 eV, enabling visible light absorption up to 470 nm. The incorporation of Zn 3d and N 2p electrons in the upper valence band creates p–d repulsion that raises the valence band maximum, effectively narrowing the band gap while maintaining strong oxidative potential. The authors systematically varied the Zn/Ga molar ratio in the starting material (0.5, 1, and 2) and found that Zn/Ga = 2 yielded the

highest photocatalytic activity for PAH degradation. Moreover, loading 0.5 wt% Pt as a cocatalyst via photodeposition (forming 1–3 nm Pt particles) dramatically enhanced activity: the initial reaction rate for phenanthrene degradation increased approximately 10-fold, and complete degradation was reported for phenanthrene, benz[a]anthracene, anthracene, and acenaphthene within 1, 3, 6, and 8 h, respectively. Comprehensive characterization of TiO_2@ZnHCF nanocomposites with enhanced photocatalytic activity, on behalf of structural modifications, provided by Rachna et al. [52] (2019) revealed that incorporation of ZnHCF into TiO_2 induced several critical modifications: (i) the band gap decreased dramatically from 3.0 eV (TiO_2) and 2.3 eV (ZnHCF) to 1.65 eV (TiO_2@ZnHCF), extending light absorption well into the visible region; (ii) BET surface area increased from 18.5 m^2/g (TiO_2) to 118.15 m^2/g (TiO_2@ZnHCF), a significant enhancement providing abundant active sites for pollutant adsorption; (iii) zeta potential became more negative (−20.5 mV to −48.2 mV), enhancing colloidal stability; (iv) PL spectroscopy showed significantly lower emission intensity for the composite, indicating suppressed electron-hole recombination. The reusability of TiO_2@ZnHCF was exceptional, with only a 7% loss in activity after ten consecutive cycles, and PXRD analysis confirmed structural integrity.

A powerful strategy for enhancing the photocatalytic activity of TiO_2 is co-doping with both metal and non-metal elements, which creates synergistic effects that surpass mono-doping. Zhao et al. [53] (2020) demonstrated this approach through the synthesis of Cu/N-codoped TiO_2 nanoparticles via a modified sol-gel method, using copper sulfate and urea as dopant sources. Comprehensive characterization revealed several critical modifications compared to pristine TiO_2 and N-doped TiO_2: (i) XRD analysis showed a decrease in crystallite size from 30 nm (TiO_2) to 14 nm (N-TiO_2) and 11 nm (Cu/N-TiO_2), indicating that both dopants retard crystal growth; (ii) UV-vis DRS revealed a progressive red shift in absorption edges from 418 nm (TiO_2) to 472 nm (N-TiO_2) to 673 nm (Cu/N-TiO_2) with corresponding band gap narrowing from 3.17 eV to 2.89 eV to 2.64 eV; (iii) BET surface area increased dramatically from 42.51 m^2/g (TiO_2) to 68.36 m^2/g (N-TiO_2) to 94.70 m^2/g (Cu/N-TiO_2), providing more active sites for pollutant adsorption; (iv) XPS analysis confirmed the incorporation of N in the TiO_2 lattice (N–Ti–O environment at 398.3 eV) and Cu as Cu_2O (Cu 2p peaks at 932.9 and 952.7 eV). The mechanism of enhancement is twofold: (i) nitrogen doping narrows the bandgap by mixing O 2p orbitals with N 2p orbitals, raising the valence band maximum; (ii) copper doping creates new energy levels below the conduction band, acting as electron traps that suppress electron-hole recombination. The synergistic effect of co-doping resulted in exceptional photocatalytic performance: Cu/N-TiO_2 achieved 96% degradation of phenanthrene under visible light within 120 min, significantly higher than N-TiO_2 (61%) and TiO_2 (<5%). The pseudo-first-order rate constant for Cu/N-TiO_2 under visible light (0.03284 min^{-1}) was approximately 22 times higher than that of TiO_2 (0.00147 min^{-1}). This study exemplifies how rational co-doping strategies can overcome the intrinsic limitations of wide-bandgap semiconductors, enabling efficient visible-light-driven photocatalysis for PAH degradation.

Qiu and Chen [55] (2024), in their study, demonstrate the photocatalytic performance of CdS/ZnO nanocomposites for PAH degradation. The authors synthesized three composites with varying Cd/Zn molar ratios (ZC-1, ZC-2, ZC-3) and characterized them using XRD, SEM, TEM, BET, FTIR, UV-vis DRS, PL, and XPS. The optimal composite, ZC-2 (Cd/Zn = 0.075:0.2), exhibited a flower-like morphology formed by needle-like structures, which enhanced pollutant adsorption and reduced incident light reflection. BET analysis revealed that ZC-2 had approximately five times higher specific surface area than pristine ZnO, providing more active sites for reaction. UV-vis DRS showed that the bandgap decreased from 3.2 eV (ZnO) to 2.4 eV (ZC-2), extending light absorption into the visible region. PL spectroscopy demonstrated that ZC-2 exhibited the lowest emission intensity,

indicating the most effective suppression of electron-hole recombination. XPS analysis confirmed the formation of a heterojunction, with binding energy shifts in Zn 2p, Cd 3d, and S 2p peaks indicating strong electronic interaction at the CdS-ZnO interface. These characterization results directly correlated with photocatalytic performance: ZC-2 achieved 98.75% degradation of naphthalene in 180 min and 96.13% degradation of anthracene in 300 min, significantly higher than pristine ZnO or CdS. After five cycles, the degradation efficiency decreased only slightly: from 98.8% to approximately 96% for naphthalene, and from 96.1% to approximately 93% for anthracene. The minor loss in activity was attributed to the accumulation of organic intermediates on the catalyst surface, which could potentially be removed through washing or mild thermal treatment.

The incorporation of graphene oxide into ZnO, by Chauhan et al. [56] (2022), resulted in several key modifications: (i) UV-vis DRS showed a red shift in the absorption edge from 354 nm (ZnO) to 376.55 nm (GO/ZnO), indicating enhanced visible light absorption; (ii) the bandgap decreased from 3.37 eV (ZnO) to 3.16 eV (GO/ZnO), as determined by Tauc plot analysis; (iii) BET surface area analysis revealed a mesoporous structure (type IV isotherm) with a surface area of 15.40 m^2/g; (iv) Raman spectroscopy confirmed the presence of defects in GO, which can serve as active sites for charge transfer. These structural modifications translated directly into enhanced photocatalytic activity: GO/ZnO achieved 86.06% degradation of phenanthrene in 120 min, compared to 62.84% for commercial ZnO under identical conditions. The pseudo-first-order rate constant for GO/ZnO (0.0375 min^{-1}) was approximately twice that of commercial ZnO (0.0186 min^{-1}). This enhancement is attributed to the synergistic effect of GO and ZnO: (i) GO acts as an electron acceptor, facilitating charge separation and reducing electron-hole recombination; (ii) the π-conjugated structure of GO enhances adsorption of phenanthrene via π-π interactions; (iii) the reduced bandgap enables more efficient utilization of visible light. This study exemplifies how rational material design combining a wide-bandgap semiconductor with a conductive carbon support can overcome intrinsic limitations of individual components. After four cycles, the degradation efficiency remained at approximately 85%, representing only a 1% loss from the initial 86.06% efficiency. This remarkable stability, maintaining >98% of initial activity after four cycles, indicates that the GO/ZnO nanocomposite retains its structural integrity and catalytic properties throughout repeated use.

A powerful strategy for enhancing photocatalytic activity is the construction of semiconductor-metal heterojunctions, which create a Schottky barrier at the interface that facilitates charge separation. Huang et al. [57] (2022) demonstrated this approach with Fe_3O_4/Cu_2O-Ag nanocomposites for PAH degradation under visible light. The key to enhanced performance lies in the difference in work functions between Cu_2O and Ag: electrons migrate from Ag (lower work function) to Cu_2O (higher work function) until Fermi level equilibration, creating a Schottky barrier that acts as an electron trap. Under visible light excitation, photoexcited electrons in the conduction band of Cu_2O transfer to Ag, where they are trapped and cannot recombine with holes. This spatial separation of charge carriers, electrons accumulated on Ag, holes remaining in Cu_2O, dramatically suppresses recombination, as confirmed by photoluminescence (PL) spectroscopy, where FCA-2 exhibited the lowest PL intensity among all samples. The trapped electrons subsequently reduce adsorbed O_2 to generate superoxide radicals ($O_2^{\bullet -}$), while holes directly oxidize PAH molecules. The optimal Ag loading (FCA-2, 2 mL $AgNO_3$) achieved >95% degradation of naphthalene within 60 min, with degradation kinetics following the order Nap (2 rings) > BaP (5 rings) > Ant (3 rings), illustrating that molecular structure influences degradation rates in a catalyst-dependent manner.

A comparative assessment of photocatalytic materials for PAH degradation, compiled by Dutta et al. [58] (2022), reveals that a combination of intrinsic material properties and architectural design governs the performance of metal oxide nanocomposites. For instance, the g-C_3N_4/Fe_3O_4 composite achieves 92% phenanthrene degradation within 120 min under visible light, attributed to the extension of light absorption into the visible region and efficient suppression of electron-hole recombination through heterojunction formation. Similarly, the TiO_2@ZnHCF nanocomposite exhibits enhanced photocatalytic activity (86% anthracene degradation under sunlight) due to its high specific surface area (118.15 m^2/g) and narrowed band gap (1.65 eV). The incorporation of Fe dopants into TiO_2 further improves visible-light activity, with 83% phenanthrene removal achieved in 2 h at alkaline pH, demonstrating that band gap engineering through doping is a viable strategy for enhancing solar-light utilization. These examples underscore that the superior performance of certain materials is not coincidental but stems from rational design principles, namely, heterojunction construction, surface area maximization, and band gap modulation that collectively reduce charge-carrier recombination and increase reactive oxygen species generation.

Wei et al. [59] (2024) in their study demonstrate the photocatalytic performance of BC@TiO_2 (BC-biochar) composites for PAH degradation. The authors employed a suite of characterization techniques to explain why the 5:1 BC:TiO_2 ratio (T2) outperformed other ratios. XPS analysis revealed the formation of Ti–O–C chemical bonds between BC and TiO_2, facilitating electron transfer. UV-vis DRS showed that BC reduced the bandgap of TiO_2 from 3.17 eV to 2.79 eV in T2, extending light absorption into the visible region. PL spectroscopy indicated that higher TiO_2 loading increased e^-/h^+ pair generation and suppressed recombination. BET surface area measurements showed that T2 had the highest specific surface area (10.75 m^2/g), providing more active sites for reaction. This multi-technique characterization approach—linking chemical bonding, band structure, charge carrier dynamics, and surface area to degradation efficiency—provides a model for rational catalyst design and enables meaningful cross-study comparisons through the use of standardized characterization protocols. An emerging perspective in environmental nanotechnology is the development of multifunctional nanomaterials that address multiple environmental and public health challenges simultaneously. Wadaan et al. [60] (2024) demonstrated that SiO_2-ZnO nanoparticles exhibit dual functionality: (i) adsorption of pyrene, a representative HMW PAH, with optimal removal of 57.39% under UV irradiation; and (ii) antibacterial activity against both Gram-positive (*S. aureus*, *B. subtilis*) and Gram-negative (*E. coli*, *K. pneumoniae*) bacteria, with zones of inhibition ranging from 11.30 to 21.57 mm at 150 µg/mL. Furthermore, the nanoparticles effectively inhibited biofilm formation (up to 65.85% for *M. luteus* at 50 µg/mL) and disrupted mature biofilms (up to 73.80% for *M. luteus*). This dual functionality is particularly relevant for environmental remediation applications where contaminated sites often harbor both organic pollutants and pathogenic microorganisms. The development of such multifunctional catalysts combining PAH adsorption/degradation with antimicrobial activity represents a promising direction for integrated remediation strategies, reducing the need for sequential treatments with different materials.

A significant advancement in heterojunction design is the S-scheme architecture, which overcomes a key limitation of traditional type-II heterojunctions, the loss of strong redox potentials. Xiao et al. [61] (2025) demonstrated this principle through the construction of TiO_2-O_v/g-C_3N_4 S-scheme heterojunction for naphthalene degradation. Using Mott-Schottky analysis, the authors determined the conduction and valence band positions of g-C_3N_4 (−1.57 eV and 1.03 eV) and TiO_2-O_v (−0.33 eV and 2.93 eV). Work function calculations revealed values of 5.3 eV for g-C_3N_4 and 6.7 eV for TiO_2-O_v, establishing that upon contact, electrons transfer from g-C_3N_4 (lower work function) to TiO_2-O_v (higher work function) until Fermi level equilibration. This creates an internal electric field at the interface. Under visible light irradiation, photogenerated electrons from the conduction band of TiO_2-O_v recombine with photogenerated holes from the valence band of g-C_3N_4, the hallmark of S-scheme charge transfer. Consequently, the remaining electrons accumulate on the more negative conduction band of g-C_3N_4, while holes accumulate on the more positive valence band of TiO_2-O_v, preserving the strong reducing and oxidizing potentials of both components. This S-scheme architecture explains the superior photocatalytic performance of TCN-30 (82.44% Nap degradation, k = 0.0102 min^{-1}) compared to pristine TiO_2-O_v (65.02%) and g-C_3N_4 (57.32%). The importance of optimal composition is underscored by the observation that 30% TiO_2-O_v loading (TCN-30) achieved maximum activity, while higher loadings reduced performance due to light blocking and inhibited g-C_3N_4 excitation.

Gonzalez Teran-Espinoza et al. [62] (2025) in their study of metal-doped lithium titanates ($Li_{0.5}TiO_2$) for phenanthrene degradation, synthesized pure LT and LT samples doped with Cu, Co, and Ni via the solvothermal method. XRD analysis confirmed the orthorhombic $Li_{0.5}TiO_2$ structure with no secondary phases, while UV-vis DRS revealed significant band gap narrowing upon metal doping: from 3.08 eV (pure LT) to 3.04 eV (LT-Cu), 2.56 eV (LT-Ni), and 2.04 eV (LT-Co). The band gap values correlated directly with photocatalytic activity: LT-Co (2.04 eV) achieved 82% phenanthrene degradation in 120 min under visible light, with a pseudo-first-order rate constant (0.01786 min^{-1}) 3.2 times higher than that of TiO_2 P25 (0.00565 min^{-1}). LT-Ni (2.56 eV) achieved 78% degradation (k = 0.01587 min^{-1}), while LT-Cu (3.04 eV) achieved only 60% degradation (k = 0.00757 min^{-1}). The superior performance of LT-Co was attributed to the ability of cobalt to act as an electron trap, suppressing e^-/h^+ recombination, and to extend photon absorption into the visible region. This study exemplifies how rational band gap engineering through metal doping, combined with careful optimization of synthesis parameters, can transform a wide-bandgap material into an efficient visible-light-active photocatalyst, outperforming conventional TiO_2 even under more energetically favorable conditions (visible vs. UV irradiation). A comprehensive overview of the photocatalytic performance of various metal oxide and heterojunction-based nanocomposites for the degradation of polycyclic aromatic hydrocarbons (PAHs) is presented in Table 4.

Table 4. Overview of structural properties and of metal oxide nanocomposites on photocatalytic performance under various conditions.

Material	Synthesis Method	Key Modifications/Structure Characteristics	Eg (eV)	S_{BET} (m^2/g)	Crystalite Size (nm)	Target PAH	Efficiency (%)	Time (min)	Light Source	k (min^{-1})	Reusability	Ref.
ZnO-based systems												
ZnO (green synthesis)	Coriandrum sativum leaf extract	Spherical NPs, phytochemical capping	–	–	9–18 (HR-TEM), 52 (DLS)	Anthracene	96	240	UV (368 nm)	0.0130	–	[39]
ZnO (chemical synthesis)	Precipitation with NaOH	Agglomerated particles	–	–	190–210	Anthracene	31	240	UV (368 nm)	–	–	
Cu@ZnO	Azadirachta indica extract, co-precipitation	Cu^{2+} doping, Schottky barrier	2.3	39.2	21.3	Naphthalene	96	200	Sunlight	0.0154 min^{-1}	9/89%	[6]
						Anthracene	94			0.01605 min^{-1}	–	
ZnO (commercial)	–	–	3.4	16	23.9	Naphthalene	79	200	Sunlight	0.00887 min^{-1}	–	
			3.4	16	23.9	Anthracene	65	200	Sunlight	0.00817 min^{-1}		
CdS/ZnO (ZC-2)	Chemical bath deposition	Type-II heterojunction, flower-like morphology	2.4	–	–	Naphthalene	98.75	180	Xe lamp (visible)	0.0214	5/96%	[55]
CdS/ZnO (ZC-2)	Chemical bath deposition	Type-II heterojunction, flower-like morphology	2.4	–	–	Anthracene	96.13	300	Xe lamp (visible)	0.0118	5/93%	[55]
GO/ZnO	Rice husk-derived GO, hydrothermal	GO incorporation, π-π interactions	3.16	15.40	–	Phenanthrene	86.06	120	UV-Vis (395 nm)	0.0375	4/85%	[56]
GaN:ZnO	NH_3 treatment of Ga_2O_3/ZnO	Solid solution, p–d repulsion	2.6	–	–	Phenanthrene	~15	60	Visible (>420 nm)	–	–	[47]
Pt-GaN:ZnO	Photodeposition of Pt (0.5 wt%)	Pt cocatalyst, electron trapping	2.6		1–3 (Pt)		100	60				
						Benz[a]anthracene	100	180				
						Anthracene	100	360				

Table 4. *Cont.*

Material	Synthesis Method	Key Modifications/Structure Characteristics	Eg (eV)	S_{BET} (m^2/g)	Crystalite Size (nm)	Target PAH	Efficiency (%)	Time (min)	Light Source	k (min^{-1})	Reusability	Ref.
TiO_2-based systems												
TiO_2	A. indica-mediated co-precipitation	Anatase/rutile mixture	3.0	18.5	–	Acenaphthene	55	1440	Sunlight	0.2091 h^{-1}	–	[52]
					–	Phenanthrene	50	1440	Sunlight	0.1268 h^{-1}		
N-TiO_2	Sol-gel	N-doping, bandgap narrowing	2.89	68.36	14	Phenanthrene	89	120	UV	0.0200	–	[53]
							61		Visible	0.00843		
Cu/N-TiO_2	Sol-gel	Co-doping (Cu + N), electron traps	2.64	94.70	11		94		UV	0.0207		
							96		Visible	0.03284		
TiO_2@ZnHCF	A. indica-mediated co-precipitation	Encapsulation, heterojunction	1.65	118.15	–	Acenaphthene	96	1440	Sunlight	0.3686 h^{-1}	10/89%	[52]
						Phenanthrene	95	1440	Sunlight	0.3310 h^{-1}	–	
BC@TiO_2	Mechanical mixing (grinding)	Ti–O–C bonds, biochar support	2.79	10.75	–	PAHs (16 total)	93.38	60	UV (254 nm)	–	–	[59]
Heterojunctions/multifunctional systems												
Fe_3O_4/Cu_2O–Ag (FCA-2)	Solvothermal + chemical deposition	Schottky barrier, SERS + photocatalysis	2.23	–	–	Naphthalene	>95	60	Visible	–	8/>90%	[57]
						Anthracene	~100	180				
SiO_2-ZnO	Chemical precipitation	Dual function (PAH + antibacterial)	–	–	85–100	Pyrene	57.39	300	UV (365 nm)	–	–	[60]
TiO_2-O_v/g-C_3N_4 (TCN-30)	Hydrothermal + calcination	S-scheme, oxygen vacancies	–	40.49	–	Naphthalene	82.44	180	Xe lamp (visible)	0.0102	4/stable	[61]
g-C_3N_4/Fe_3O_4	Calcination (melamine, 550 °C) + in situ co-precipitation	Heterojunction, Fe_3O_4 as electron acceptor	–	–	~20 (Fe_3O_4)	Phenanthrene	92.3	120	Visible	–	–	[63]

Note: Eg—bandgap energy; SBET—BET specific surface area; PAH—polycyclic aromatic hydrocarbons; k—pseudo-first-order rate constant; NPs—nanoparticles; GO—graphene oxide; O_v—oxygen vacancies; "–"—not reported.

4.2. The Influence of Operational Conditions and Water Matrix Composition on Photocatalytic Efficiency

The influence of operational parameters on photocatalytic PAH degradation is presented in detail by Brindhadevi et al. [64] (2024), who used hausmannite (Mn_3O_4) nanoparticles in water and soil matrices. The authors systematically evaluated four key parameters: initial PAH concentration, catalyst dosage, pH, and irradiation source. Increasing initial PAH concentration from 2 to 10 µg/mL reduced degradation efficiency from 67.2% to 41.2% in water, attributed to the limited availability of active sites and insufficient •OH radicals relative to pollutant molecules. Conversely, increasing the catalyst dosage from 2 to 10 µg/mL enhanced degradation from 26.9% to 66.1%, due to increased surface area and active-site availability. pH exhibited a strong influence: lower pH (5–7) favored degradation in soil, while neutral to slightly alkaline pH (7–9) was optimal in water. This pH dependence was explained by protonation of surface functional groups and the resulting changes in surface charge and polarity. Irradiation studies confirmed that UV light was more effective than sunlight, with degradation increasing up to 360 min before declining due to accumulation of intermediates and radical recombination. These results provide a significant insight for future testing of photocatalytic degradation of PAHs such as anthracene and phenanthrene.

The influence of solution pH on photocatalytic PAH degradation was systematically investigated by Chauhan et al. [56] (2022) using GO/ZnO nanocomposites for phenanthrene removal. Over a pH range of 3 to 11, degradation efficiency varied dramatically: from only 15.06% at pH 3 to 41.22% at pH 4.3, 86.06% at neutral pH (6.8), and reaching a maximum of 96.44% at pH 10.5. This pH-dependent behavior can be explained by several factors. First, at acidic pH, the positively charged surface of the photocatalyst repels phenanthrene molecules (which are neutral but have high π-electron density), limiting adsorption. Second, at basic pH, the surface becomes negatively charged, promoting the formation of "cation-π" complexes between the catalyst surface and the π-electron-rich aromatic rings of phenanthrene, enhancing adsorption and subsequent degradation. Third, the generation of hydroxyl radicals (•OH)—the primary oxidizing species, is favored at higher pH due to the abundance of OH^- ions. However, it is noteworthy that the optimal pH for practical applications may differ from the maximum efficiency pH; the authors selected pH 6.8 (the unadjusted natural pH) as the optimal condition for subsequent experiments, balancing efficiency with the cost of pH adjustment.

The influence of operational parameters on photocatalytic efficiency is evident from the study of Fe-doped TiO_2, where alkaline conditions (pH > 7) were found to enhance phenanthrene degradation significantly [58]. This observation underscores the need for systematic investigation of water matrix components, such as inorganic ions (chlorides, carbonates, sulfates) and natural organic matter, that can scavenge reactive oxygen species or alter catalyst surface charge, thereby modulating degradation kinetics and product distribution. Natural organic matter also presents an issue since it can adsorb onto catalyst surfaces, blocking active sites and reducing photocatalytic efficiency. Furthermore, the variable pH, ionic strength, and turbidity of real effluents affect catalyst stability, light penetration, and radical generation. These challenges are compounded by the fact that most photocatalytic studies are conducted under idealized conditions, deionized water, controlled pH, and single-pollutant systems that do not reflect the complexity of real wastewater matrices [54].

A critical parameter influencing photocatalytic efficiency is the concentration of dissolved oxygen (DO), which serves as the primary electron acceptor in semiconductor photocatalysis. Azim et al. [65] (2024) systematically investigated this effect, demonstrating a direct correlation between DO concentration and degradation performance. As DO concentration increased from 2.8 to 3.9 mg/L, the degradation efficiency of the GO sys-

tem improved from 36% to 78%, while the pseudo-first-order rate constant (k) increased from 0.0074 to 0.025 min^{-1}. In the H_2O_2-assisted system (GO + H_2O_2), the rate constant increased from 0.035 to 0.062 min^{-1} (1.8-fold enhancement) under the same DO range. The mechanistic role of dissolved oxygen is twofold: (i) photogenerated electrons (e_{CB}^-) are captured by adsorbed O_2 molecules to form superoxide radicals ($O_2^{\bullet-}$), which directly participate in pollutant degradation and simultaneously suppress electron-hole recombination; (ii) oxygen vacancies on the catalyst surface act as electron sinks, facilitating charge separation and enhancing the yield of reactive oxygen species. These findings underscore that DO is not merely a passive component but an active participant in photocatalytic reactions, and its concentration must be considered when optimizing treatment systems. The positive correlation between DO and degradation efficiency highlights the importance of maintaining adequate aeration in photocatalytic reactors, particularly for field-scale applications where natural oxygen levels may be limiting. The importance of the influence of water matrix composition on AOP efficiency is discussed by Rubio-Clemente et al. [66] (2018), who compared the UV/H_2O_2 degradation of anthracene (AN) and benzo[a]pyrene (BaP) in natural surface water (NW) versus deionized water (DW). While both matrices achieved >99.8% removal of the parent compounds under optimal conditions (11 mg/L H_2O_2, 0.63 mW/cm^2 UV-C irradiance), the degradation kinetics were notably slower in NW. The authors attributed this to the presence of natural organic matter (NOM, TOC = 2.03 mg/L) and inorganic anions (Cl^-, HCO_3^-, CO_3^{2-}, SO_4^{2-}, PO_4^{3-}) in the natural water, which act as $^{\bullet}OH$ scavengers and reduce UV penetration via the inner filter effect. Under optimal UV/H_2O_2 conditions, AN and BaP removal exceeded 99.8% within 2–15 min, yet total organic carbon (TOC) removal reached only 61.2% after 90 min and 69.3% after 120 min. This substantial gap between parent compound degradation and mineralization indicates the accumulation of transformation products identified as quinones (anthracene-9,10-dione, benzo[a]pyrene-4,5-dione), hydroxylated aromatics, and carboxylic acids that persist in the water matrix. The presence of these intermediates, despite the high $^{\bullet}OH$ flux, underscores that mineralization requires significantly more oxidative energy than initial ring cleavage.

The influence of matrix composition on photocatalytic efficiency is indirectly illustrated by the work of Wei et al. [59] (2024), who investigated PAH degradation in biochar—a complex carbonaceous matrix containing persistent free radicals (PFRs), oxygen-containing functional groups, and inorganic elements. The authors found that biochar itself acted as a co-catalyst, with phenol and quinone groups facilitating electron transfer and contributing to $O_2^{\bullet-}$ generation. This intrinsic catalytic activity of the matrix, distinct from the added TiO_2 highlights a key consideration for real-world applications: the matrix itself may either enhance or inhibit photocatalytic performance depending on its composition. Kavitha et al. [67] (2026) addressed realistic environmental scenarios involving complex mixtures of contaminants rather than single pollutants by investigating the photocatalytic degradation of a ternary PAH mixture: naphthalene (NAP), anthracene (ANT), and benzo[a]pyrene (BaP); over CeO_2 nanoparticles under sunlight. GC-MS analysis revealed that despite the structural diversity of the parent compounds, degradation converged toward common intermediates: Phthalic acid, catechol, salicylic acid, and short-chain aldehydes and acids. Interestingly, the presence of BaP—a high-molecular-weight PAH with five aromatic rings—appeared to influence the surface strain of the catalyst, as evidenced by Williamson-Hall analysis showing tensile strain for the ternary mixture compared to compressive strain for single PAHs. This observation suggests that competitive adsorption and differential reactivity of co-contaminants can alter the catalyst surface state and potentially influence degradation kinetics.

Beyond conventional photocatalysis, hybrid advanced oxidation processes offer complementary degradation pathways that can overcome the limitations of single-technique approaches. The combination of UV radiation with ozone (UV/O_3) or hydrogen peroxide (UV/H_2O_2) significantly enhances $^{\bullet}OH$ generation compared to photolysis alone. However, the effectiveness of these hybrid systems is highly dependent on the chemical structure of the target PAH; for instance, while UV/O_3 improved the degradation of chrysene, it showed no synergistic effect for fluoranthene. The photo-Fenton process, which couples Fenton chemistry with UV/visible light, offers the additional advantage of Fe^{2+} regeneration and can operate under solar radiation, reducing operational costs [68]. As demonstrated by Abd Manan et al. [69] (2019), the photo-Fenton system operates through a synergistic mechanism: UV light (365 nm) promotes the photoreduction of Fe^{3+} to Fe^{2+}, regenerating the catalyst and sustaining $^{\bullet}OH$ production via the classical Fenton reaction. This combination overcomes a key limitation of conventional Fenton treatment—the accumulation of Fe^{3+} and the associated sludge formation, while also enabling higher $^{\bullet}OH$ yields than either process alone. The authors achieved 76–91% removal of 17-US EPA PAHs from real potable water samples within 150 min, with TOC removal reaching up to 99%. Importantly, the process was optimized using response surface methodology (RSM), revealing that pH and the H_2O_2:$FeSO_4$ molar ratio (MR) were the most critical parameters, with optimal values of pH 4.65 and MR 0.12. These findings illustrate that photo-Fenton is a viable alternative to conventional water treatment for PAH-contaminated water, particularly in settings where existing infrastructure fails to remove these persistent organic pollutants.

A systematic investigation of the influence of operational parameters on PAH degradation was conducted by Zheng et al. [70] (2024) in a Fe_3O_4-nZVI Fenton-like system. Their results demonstrate that each parameter exhibits a characteristic optimum beyond which degradation efficiency declines. H_2O_2 concentration—the primary source of $^{\bullet}OH$—showed an optimal range of 10–15 mmol/L; excess H_2O_2 acted as a $^{\bullet}OH$ scavenger and underwent catalase-like decomposition, reducing radical availability. Catalyst dosage (Fe_3O_4-nZVI) exhibited a similar pattern, with 0.6 g/L identified as optimal; higher loadings led to Fe^{2+}-mediated $^{\bullet}OH$ scavenging and surface passivation by iron hydroxide precipitation. The system was strongly pH-dependent, with maximum efficiency at pH 3. At lower pH, $^{\bullet}OH$ was consumed by H^+, while at higher pH, Fe^{2+} became unstable and precipitated as $Fe(OH)_3$. Temperature optimization revealed an optimum at 25–35 °C; higher temperatures accelerated H_2O_2 decomposition and promoted catalyst passivation. These findings underscore that photocatalytic system optimization requires systematic evaluation of interdependent parameters, as performance is governed not by individual factors but by their interactive effects on radical generation, scavenging, and catalyst stability.

Bendouz et al. [71] (2016) systematically optimized this process for three representative PAHs—phenanthrene (Phe), fluoranthene (Fle), and benzo[a]pyrene (BaP)—demonstrating that degradation efficiency is strongly dependent on H_2O_2 concentration, temperature, and reaction time. Optimal conditions (15 g/L H_2O_2, H_2O_2:Fe^{2+} molar ratio 10:1, pH 2.5, 60 °C) yielded >99% degradation of Phe and Fle, and 90% degradation of BaP within 180 min. Importantly, the process achieved 66–73% total organic carbon (TOC) removal within 30 min, indicating substantial mineralization alongside parent compound degradation. Kinetic analysis revealed pseudo-first-order behavior, with rate constants increasing from 0.048 min^{-1} at 20 °C to 0.097 min^{-1} at 60 °C for Phe. While Fenton oxidation is highly effective, its practical application is constrained by the narrow optimal pH range (2.5–3.0), the generation of iron sludge requiring disposal, and the consumption of stoichiometric amounts of H_2O_2. In contrast, photocatalytic systems—particularly those employing immobilized or magnetic catalysts (e.g., Fe_3O_4-nZVI)—offer the advantages of catalyst

reusability, broader pH operability, and the potential for solar light utilization, albeit often with lower mineralization rates.

Dutta et al. (2022) [58] identify several critical challenges that must be addressed for the sustainable deployment of photocatalytic nanomaterials in PAH remediation. Primary among these is the potential for secondary contamination, as nanoparticles can act as carriers of PAHs and heavy metals in soil matrices, and the inherent toxicity of nanomaterials themselves to non-target organisms such as earthworms and other soil biota. Furthermore, high degradation efficiencies (>90%) do not necessarily correlate with complete detoxification; therefore, comprehensive toxicological assessment—including pre- and post-treatment evaluations is imperative. The authors also caution that nanoparticle addition can alter soil pH and physical properties, with potential adverse effects on indigenous microbial communities. These considerations highlight the necessity of integrating life-cycle assessment and ecotoxicological endpoints into the design and evaluation of photocatalytic systems, moving beyond the current focus on degradation percentages alone.

A critical insight from the study by Abd Manan et al. [69] (2019) is the distinction between PAH degradation and complete mineralization. While the photo-Fenton process achieved 76–91% removal of 17 USEPA PAHs from potable water samples, the corresponding TOC removal ranged from 76% to 99%, with significant variation between sampling sites. For instance, at the WTPP site, PAH removal was 91% but TOC removal was only 76%, indicating that transformation products accounted for approximately 15% of the residual organic carbon. This discrepancy underscores a key point raised throughout this review: monitoring the disappearance of parent PAH compounds is insufficient to guarantee detoxification. Transformation products—such as quinones, phthalates, and hydroxylated intermediates—may persist and exhibit toxicity profiles comparable to or exceeding those of the parent compounds. Bendouz et al. [71] (2016) provide a compelling illustration of the distinction between parent compound disappearance and genuine mineralization: while Fenton oxidation achieved 90–99% removal of individual PAHs under optimized conditions, TOC removal ranged from 66% to 73% after 30 min, indicating that a significant fraction of organic carbon remained as transformation products. GC-MS analysis identified these intermediates as phthalic anhydride, phthalic acid, benzoic acid, and various hydroxylated aromatic compounds—many of which exhibit toxicity profiles that differ from parent PAHs. Therefore, future studies should adopt TOC removal and toxicity bioassays as complementary metrics to parent compound degradation, ensuring that photocatalytic treatment achieves genuine environmental detoxification rather than mere pollutant transformation. Xiao et al. [61] (2025) identified a substantial gap between parent compound degradation and mineralization. While the TCN-30 S-scheme heterojunction achieved 82.44% degradation of naphthalene within 180 min, total organic carbon (TOC) removal reached only 12.26% under identical conditions. This disparity indicates that while the aromatic rings of naphthalene are effectively cleaved—as confirmed by LC-MS identification of intermediates—the resulting smaller organic fragments accumulate in solution rather than being fully mineralized to CO_2 and H_2O. The authors observed that TOC removal accelerated after 60 min, coinciding with the transition from naphthalene macromolecules to smaller intermediates, suggesting that mineralization becomes more efficient once the initial ring-opening step is complete.

From a practical perspective, the translation of photocatalytic nanomaterials from laboratory-scale studies to field applications faces substantial hurdles. The complexity of real environmental matrices characterized by variable pH, ionic strength, and natural organic matter can dramatically alter radical chemistry and catalyst stability, yet most studies remain confined to idealized conditions. Moreover, the economic viability of

nanomaterial synthesis and the potential for nanoparticle release into the environment necessitate rigorous cost-benefit and life-cycle analyses.

5. Insights into Roles of Superoxide and Non-Radical Oxygen Species in Photocatalytic Degradation

In heterogeneous photocatalytic systems for low-molecular-weight PAHs such as anthracene, the oxidation mechanism under UV-excited wide-bandgap oxides (TiO_2, ZnO) proceeds via photogenerated holes (h^+) that generate hydroxyl radicals ($^\bullet OH$) through oxidation of surface OH^- or H_2O. These $^\bullet OH$ radicals act as the dominant oxidizing species, attacking the aromatic ring to yield oxygenated products. For anthracene on both TiO_2 (P25) and ZnO under UV irradiation, 9,10-anthraquinone is consistently identified as the major early-stage degradation product [39,72], consistent with a pathway involving $^\bullet OH$-mediated aromatic hydroxylation followed by rapid progression to quinones. The kinetic data in both studies follow pseudo-first-order behavior, and no evidence of alternative oxidant-assisted regimes (e.g., persulfate or peroxymonosulfate) was examined; thus, the reported mechanisms reflect canonical UV-photocatalysis in the absence of added oxidants. A recurring limitation in interpreting photocatalytic PAH degradation is the tendency to attribute all oxidative activity to hydroxyl radicals, while treating superoxide radicals, photogenerated holes, and singlet oxygen as secondary or negligible contributors. The literature reviewed here, however, reveals a more nuanced picture in which the relative contribution of each species is strongly catalyst-dependent and cannot be generalized across systems. Under visible-light "hybrid AOP" conditions, the oxidant palette broadens: in a Co/Ce–TiO_2 system activating peroxymonosulfate (PMS) for phenanthrene degradation, quenching experiments and Electron Spin Resonance (ESR) spectroscopy verified the involvement of h^+, $O_2^{\bullet-}$, and $^1O_2$ alongside the sulfate-radical chemistry intrinsic to PMS, emphasizing that non-radical oxygen species ($^1O_2$) can become non-negligible when oxygen activation pathways are promoted [73].

Qiu and Chen [55] (2024) employed radical quenching experiments with EDTA (h^+ scavenger), benzoquinone (BQ, $O_2^{\bullet-}$ scavenger), and tert-butanol (TBA, $^\bullet OH$ scavenger) to elucidate the dominant ROS in CdS/ZnO-mediated PAH degradation. The results showed that the addition of BQ or EDTA dramatically suppressed degradation efficiency, while TBA had only a minor effect, confirming that superoxide radicals ($O_2^{\bullet-}$) and photogenerated holes (h^+) were the primary reactive species, with hydroxyl radicals ($^\bullet OH$) playing a secondary role. This finding is consistent with the type-II heterojunction mechanism, where electrons accumulate on the ZnO conduction band and reduce O_2 to $O_2^{\bullet-}$, while holes accumulate on the CdS valence band and directly oxidize PAH molecules. Kinetic analysis using the pseudo-first-order model yielded excellent fits ($R^2 > 0.98$), with rate constants of 0.0214 min^{-1} for naphthalene and 0.0118 min^{-1} for anthracene—3–4 times higher than pristine ZnO or CdS.

Fischer et al. [74] (2024) demonstrated that $O_2^{\bullet-}$, formed as a byproduct of $^\bullet OH$ -initiated benzyl alcohol oxidation, acts as a potent nucleophile that attacks α,β-unsaturated carbonyl intermediates (e.g., 5-hydroxy-4-oxo-pentenal) via conjugate addition. This initiates radical chain reactions that cleave C–C bonds to yield oxalic and formic acids, while regenerating $O_2^{\bullet-}$ without consuming $^\bullet OH$. Critically, these reactions require a protic solvent to stabilize the charged superoxide species, highlighting the unique role of aqueous environments in promoting non-radical oxygen species pathways. Although these findings originate from sonochemical systems, they provide mechanistic evidence that $O_2^{\bullet-}$ is not merely a secondary radical but can actively participate in propagating the degradation of ring-opening products, thereby preserving $^\bullet OH$ for the initial activation of refractory aromatic pollutants such as PAHs.

The role of superoxide in advanced oxidation processes extends beyond that of a secondary species. In ozonation systems, Guo et al. [75] (2023) quantitatively demonstrated that $O_2^{\bullet-}$ acts as a chain carrier, contributing 45–70% of overall ozone decomposition depending on water matrix composition, with the remainder attributed to direct reactions with $^{\bullet}OH$, OH^-, and dissolved organic matter. Using CCl_4 as a selective probe for $O_2^{\bullet-}$ and pCBA for $^{\bullet}OH$, the authors derived exposure ratios (RSO and RSH) analogous to the well-established Rct concept, enabling quantitative comparison of reactive species contributions. These findings underscore that in aqueous AOP systems, the relative importance of $O_2^{\bullet-}$ can rival or even exceed that of $^{\bullet}OH$, challenging the common practice of treating superoxide as a minor contributor. Moreover, the strong dependence of $O_2^{\bullet-}$ contribution on the presence of promoters (e.g., methanol) versus inhibitors (e.g., carbonate, acetate) highlights that the operant oxidant hierarchy is inherently conditional on water composition. While these insights originate from ozonation, the methodological framework, particularly the use of selective probes and exposure-based kinetic modeling, is directly transferable to photocatalytic systems, where similar quantitative assessments of $O_2^{\bullet-}$ contributions remain largely absent.

In UV-excited photocatalysis on TiO_2, the formation of both hydroxyl radicals and superoxide is well established, as illustrated by Karam et al. [72] (2014) for anthracene degradation. Following band gap excitation, photogenerated electrons reduce O_2 to $O_2^{\bullet-}$, while valence band holes oxidize surface OH^- or H_2O to $^{\bullet}OH$. The latter is widely considered the dominant oxidizing species, consistent with the identification of 9,10-anthraquinone as the major early degradation product—a transformation pathway that proceeds via $^{\bullet}OH$-mediated aromatic hydroxylation followed by oxidation to the quinone. Although superoxide is produced in such systems, its contribution to pollutant abatement in conventional UV-TiO_2 photocatalysis is often regarded as secondary, particularly in the absence of external oxidants or promoters.

A systematic review by Chauhan et al. [49] (2021) on photocatalytic degradation of phenanthrene compiled the dominant reactive oxygen species for many different photocatalyst systems. While $^{\bullet}OH$ is frequently cited as the primary oxidant in canonical UV-TiO_2 photocatalysis, the review highlights that the contribution of $O_2^{\bullet-}$ can be substantial and even dominant in certain systems. For instance, in a GO-TiO_2-$Sr(OH)_2$/$SrCO_3$ composite under UV irradiation, scavenger experiments revealed that $O_2^{\bullet-}$ accounted for approximately 77% of the observed phenanthrene degradation, far exceeding the contribution of $^{\bullet}OH$ (63%) or $^1O_2$ (51%). Moreover, the review compiles evidence that hybrid systems incorporating peroxymonosulfate (PMS) or persulfate broaden the oxidant palette to include $SO_4^{\bullet-}$ alongside $^{\bullet}OH$ and $O_2^{\bullet-}$, as observed in FeCo-BDC/PMS and SSNT@GQD/persulfate systems. These findings collectively underscore that the operant oxidant hierarchy in photocatalytic PAH degradation is inherently conditional—dependent on catalyst composition, the presence of external oxidants, and the specific reaction environment—challenging the oversimplified view that hydroxyl radicals are universally the dominant species.

The temporal dynamics of photoproduct formation in UV-TiO_2 systems were systematically investigated by St. Mary et al. [76] (2021) for anthracene and phenanthrene. Using a combination of GC-MS analysis, oxidative potential measurements (DTT assay), and gene expression profiling in larval zebrafish, the study revealed that hydroxylation is the initial photochemical event, with OHPAHs appearing within the first hour of irradiation and subsequently decreasing as OPAHs accumulate over time. Notably, the presence of TiO_2 nanoparticles promoted the formation of 1-hydroxynaphthalene via reaction of photogenerated $^{\bullet}OH$ radicals with photodissociated fragments. Critically, the study identified OPAH photoproducts larger than the parent PAH molecules (e.g., BaP-dienes,

6H-benzo(cd)pyrene-6-one), suggesting that photodissociation followed by recombination and ring rearrangement can occur alongside oxidative degradation. These findings challenge the assumption that photocatalysis invariably leads to complete mineralization and highlight that complex, potentially more toxic transformation products may form. Furthermore, the study demonstrated PAH-specific effects: while TiO_2 sustained the oxidative potential of anthracene over time, it reduced that of phenanthrene—an observation attributed to differences in UVA absorption and surface adsorption affinities. This underscores that the efficacy and mechanism of photocatalytic PAH degradation are inherently compound-dependent.

The role of superoxide as a dominant oxidant in photoelectrocatalytic systems was convincingly demonstrated by Qiao et al. [77] (2017) using TiO_2 nanotubes for anthracene degradation. Electron spin resonance (ESR) spectroscopy confirmed the generation of both $O_2^{\bullet-}$ and $^{\bullet}OH$, while scavenger experiments revealed that the addition of benzoquinone (a $O_2^{\bullet-}$ quencher) nearly completely suppressed the formation of anthranone and anthraquinone, the major oxygenated intermediates, and significantly reduced anthracene elimination. In contrast, quenchers for $^{\bullet}OH$ (tert-butanol) and photogenerated holes (EDTA-2Na) had only marginal effects. These findings demonstrate that, under photoelectrocatalytic conditions, $O_2^{\bullet-}$ is not merely a secondary species but the primary reactive oxygen species driving both the initial transformation of the parent PAH and the formation of oxygenated products. Notably, the intermediates anthranone and anthraquinone accumulated over time without further degradation within the experimental timeframe, highlighting that photoelectrocatalytic treatment may lead to the persistence of transformation products that are themselves of toxicological concern. The study further showed that the photoelectrocatalytic process achieved higher elimination efficiency than conventional photocatalysis, electrochemical oxidation, or direct photolysis, while consuming significantly less energy than UV-based photocatalytic systems—underscoring the potential of PEC as both an efficient and energy-sustainable approach for PAH remediation.

The hierarchy of oxidative species in the photocatalytic degradation of PAHs is not universal but rather conditional—it depends on the type of photocatalyst, the presence of added oxidants (PMS, persulfate), the applied electrical potential (in the case of PEC), the composition of the aqueous matrix, as well as the structure of the PAH itself. Depending on these factors, superoxide radicals can be the dominant species, a chain carrier in radical chains, or negligible, necessitating abandoning the simplistic model in which the hydroxyl radical is always and solely responsible for degradation. Future research should integrate quantitative methods to assess the contributions of different ROS (ESR, selective probes, kinetic modeling) to develop predictive frameworks for optimizing photocatalytic water treatment.

6. Environmental Relevance and Toxicity Considerations

The identification of degradation intermediates by GC-MS and LC-MS constitutes a necessary but insufficient criterion for evaluating photocatalytic treatment efficacy. A critical question, whether photocatalytic degradation achieves genuine detoxification or merely transforms one class of hazardous compounds into another, requires integrating structural identification with ecotoxicological data. This distinction is particularly important for PAHs, where certain oxygenated intermediates can exhibit toxicity profiles that differ markedly from, or even exceed, those of the parent compounds. The formation of 9,10-anthraquinone as the primary stable intermediate of anthracene degradation has been widely interpreted as a detoxification step, and available ecotoxicity data support this interpretation: the acute oral LD_{50} for anthraquinone in rats and mice exceeds 5000 mg/kg, is significantly lower than that of anthracene (LD_{50} > 16.000 mg/kg for rats and mice) [78,79].

Ecotoxicological evaluation of key transformation products reveals marked differences in hazard profiles. Tukaj and Aksmann [80] (2007) determined the acute toxicity of 9,10-anthraquinone and 9,10-phenanthrenequinone to the green alga *Scenedesmus armatus*, reporting EC_{50} values of 0.56 mg dm^{-3} and 0.10 mg dm^{-3}, respectively. Notably, while anthraquinone exhibited approximately half the toxicity of its parent anthracene, phenanthrenequinone was found to be 100 times more toxic than phenanthrene. This striking disparity underscores that the formation of oxygenated intermediates does not inherently constitute detoxification; rather, the toxicological outcome is highly compound-specific. Furthermore, the study revealed strain-specific sensitivity to anthraquinone, with one *Scenedesmus* strain showing complete resistance, highlighting that ecotoxicological responses can vary even within the same species.

The toxicity profile of anthrone, a key intermediate in anthracene photodegradation, is markedly different from that of its parent compound. Anthrone is classified under the EU CLP regulation as a skin and eye irritant (H315, H319) and a respiratory tract irritant (H335), but not as acutely toxic, carcinogenic, mutagenic, or reproductively toxic [81]. Ecotoxicologically, anthrone is not classified as hazardous to the aquatic environment and does not significantly bioaccumulate (log K_ow = 3.66). This stands in contrast to anthracene, which exhibits high acute toxicity to aquatic organisms (LC_{50} for bluegill sunfish = 0.001 mg/L) and is listed as a priority hazardous substance under the Water Framework Directive. The available data thus support the interpretation that the conversion of anthracene to anthrone—and further oxidation to 9,10-anthraquinone—represents a genuine detoxification step, although careful attention must be paid to the specific transformation pathway and the potential persistence of intermediates under different environmental conditions.

Phthalic acid, a common terminal intermediate in the photocatalytic degradation of both anthracene and phenanthrene, belongs to the broader class of phthalic acid esters (PAEs)—environmental endocrine disruptors that have been classified as priority pollutants by the US EPA and as substances of very great concern under the EU REACH regulation. While the acute toxicity of phthalic acid is lower than that of its ester derivatives, the regulatory concern stems from chronic exposure effects, including reproductive toxicity, neurodevelopmental impairment, and potential carcinogenicity associated with long-chain phthalates [82,83]. Although phthalic acid itself exhibits a more favorable toxicological profile—consistent with its classification as non-hazardous to the aquatic environment—its presence as a degradation product should not be interpreted as evidence of complete detoxification without complementary ecotoxicity testing.

The toxicological profile of phthalic acid can be informed by the extensive risk assessment of its diester derivative, DEHP, conducted by the European Union (EU RAR, 2008) [84]. DEHP exhibits pronounced reproductive and developmental toxicity, with a NOAEL of 4.8 mg/kg bw/day established in a three-generation rat study based on testicular atrophy, reduced anogenital distance, and feminization of male offspring. The active metabolite MEHP directly targets Sertoli cells, disrupting FSH-stimulated cAMP accumulation and germ cell adhesion. While the hepatocarcinogenic effects of DEHP in rodents (mediated by PPARα activation) are considered not relevant to humans due to low PPARα expression in human liver, the reproductive and developmental effects are recognized as relevant endpoints for human risk assessment. Consequently, DEHP is classified under EU legislation as toxic to reproduction (Category 2; R60-61). By extension, the presence of phthalic acid as a degradation product warrants careful evaluation, as it represents the terminal hydrolytic product of a substance class with well-documented endocrine-disrupting properties. Although phthalic acid itself exhibits lower acute toxicity than its diesters, its potential for conversion back to monoesters under biological condi-

tions or its role as a marker of exposure to reprotoxic phthalates necessitates inclusion in post-treatment monitoring.

3-Hydroxy-2-naphthoic acid, identified as a key intermediate in the photocatalytic degradation of both anthracene and phenanthrene, exhibits a toxicological profile that warrants consideration in the assessment of treatment efficacy. According to its Safety Data Sheet [85], the compound is classified under the EU CLP regulation as harmful to aquatic life with long-lasting effects (H412). Notably, it is not classified as carcinogenic, mutagenic, or reproductively toxic, and it is not listed as a Substance of Very High Concern (SVHC) under REACH. However, its log K_ow of 3.05 indicates moderate lipophilicity, suggesting potential for bioaccumulation, while its water hazard classification (WGK 2, "significantly hazardous to water") underscores that its release into aquatic environments should be minimized. These findings demonstrate that while 3-hydroxy-2-naphthoic acid is less hazardous than the parent PAHs in certain respects, its chronic aquatic toxicity and eye/skin irritation potential necessitate its inclusion in the risk assessment of photocatalytic treatment processes.

A critical insight from photodegradation studies of structurally related PAHs is that the toxicity of reaction mixtures is not solely determined by the residual parent compound. Kang et al. (2019) [86] demonstrated that during the photodegradation of naphthalene and alkylated naphthalenes, the overall toxicity—assessed by the luminescence inhibition of *Aliivibrio fischeri*—consistently exceeded the toxicity accounted for by the remaining parent compounds. The contribution of transformation products to the total toxic units (TU) increased with reaction time, reaching up to 47% for naphthalene after 6 h of irradiation. Importantly, the authors observed a transient increase in toxicity during the initial stages of photodegradation, attributed to the formation of oxygenated intermediates such as naphthols, naphthaldehydes, and naphthoquinones—compound classes that are also prominent in the degradation pathways of anthracene and phenanthrene. These findings underscore that the evaluation of photocatalytic treatment efficacy must extend beyond monitoring the disappearance of the parent PAH; it requires the integration of chemical analysis with ecotoxicity assays to capture the dynamic hazard profile of transformation products.

Maleic acid, a dicarboxylic acid that can arise from the further oxidation of phthalic acid or as a ring-opening product during the photocatalytic degradation of PAHs, exhibits a distinct toxicological profile. According to the safety assessment by the Cosmetic Ingredient Review [87], maleic acid is not mutagenic in standard Ames tests (negative up to 7500 µg/plate) and is not classified as a carcinogen. However, it demonstrates significant nephrotoxicity in animal models, inducing Fanconi syndrome—characterized by glucosuria, aminoaciduria, and phosphaturia—at intraperitoneal doses as low as 1.5 mmol/kg in rats, with inhibition of proximal tubule NaK-ATPase (80%) and H-ATPase (50%) identified as the underlying mechanism. Ocular exposure to a 10% solution (pH 1.0) for 30 s caused permanent corneal opacity in rabbits, while dermal application of 20% maleic acid (pH 1.4) for six weeks induced acute vesicular dermatitis in 34% of human volunteers. Importantly, the toxicity of maleic acid is strongly pH-dependent; at neutral pH, as maleate salts, the compound exhibits significantly lower irritancy. In the context of photocatalytic treatment, where maleic acid may form as a transient intermediate, its potential for renal and dermal toxicity underscores the necessity of achieving complete mineralization rather than partial oxidation to dicarboxylic acids that retain bioactivity.

The evidence assembled does not diminish the promise of photocatalysis for PAH remediation. Rather, it reframes the challenge: true environmental protection requires not merely the transformation of parent pollutants but the predictable and complete mineralization of both parent compounds and their intermediates. The mechanistic insights into superoxide propagation, the quantitative frameworks for ROS contribution, and the

toxicological profiles of key intermediates assembled in this review collectively provide the foundation for the rational design of next-generation photocatalytic systems. Future research must embrace the complexity inherent in real environmental systems. The conditional nature of the oxidant hierarchy—where the relative contributions of $^{\bullet}OH$, $O_2^{\bullet-}$, $^1O_2$, and h^+ depend on catalyst composition, water matrix, and operational parameters—demands a shift from empirical optimization toward mechanistic understanding. The integration of computational materials design, advanced spectroscopic characterization, and ecotoxicological validation offers a pathway toward photocatalytic systems that reliably achieve the ultimate goal: the conversion of persistent organic pollutants to CO_2 and H_2O without the accumulation of intermediates whose hazards exceed those of the parent compounds.

7. Current Limitations and Future Perspective

A cross-sectional analysis of the reviewed literature reveals several recurring patterns governing photocatalytic performance in both anthracene and phenanthrene systems, regardless of the specific catalyst employed. The oxidative entry point is remarkably consistent: hydroxyl radical attack preferentially targets the C9 and C10 positions in both compounds, with quinone-type intermediates—particularly 9,10-anthraquinone and phenanthrenequinone—emerging as the dominant early-stage products across virtually all catalyst systems reviewed. This mechanistic convergence, while reflecting the inherent chemical reactivity of the K-region in peri-condensed PAHs, also implies that intermediate ecotoxicity rather than parent compound persistence may be the rate-limiting concern in treatment scenarios, a point insufficiently addressed in most of the reviewed studies. Nanocomposite and heterojunction-based systems consistently outperform single-component metal oxides, with the performance advantage attributable primarily to three interconnected factors: suppressed electron-hole recombination, increased active surface area, and extended light absorption into the visible range. However, the magnitude of this improvement varies considerably depending on synthesis method, dopant concentration, and irradiation conditions. It rarely follows a predictable trend across different studies, reinforcing the need for more standardized comparative frameworks. Among operational parameters, pH emerges as one of the most influential, yet its optimal range is catalyst-specific rather than universal. Acidic to near-neutral conditions generally favor degradation for TiO_2- and ZnO-based systems through favorable surface charge interactions, but the mechanistic rationale is often incompletely reported. Similarly, catalyst loading shows a consistent saturation effect across all reviewed systems, beyond which light scattering and reduced photon penetration offset the benefit of additional active sites. These patterns suggest that operational optimization cannot be generalized across catalyst classes and must be addressed system-specifically in future work.

Finally, a critical gap that runs through the entire reviewed literature concerns the absence of integrated ecotoxicological assessment alongside degradation efficiency data. The transformation of anthracene and phenanthrene into quinone intermediates does not guarantee reduced environmental hazard—some hydroxylated and quinone derivatives exhibit comparable or enhanced biological activity relative to the parent compounds. Progress in this field will require a shift from efficiency-centered reporting toward outcome-based evaluation frameworks that couple degradation kinetics with toxicity monitoring of the full intermediate profile.

A critical methodological consideration that warrants explicit acknowledgment concerns the potential contribution of direct photolysis and photosensitization effects to the observed degradation efficiencies. Given the well-documented light-absorbing properties of PAHs in the UV–visible range, a fraction of the reported degradation may, in some

studies, reflect non-catalytic photochemical pathways rather than purely heterogeneous photocatalytic mechanisms. This issue is particularly relevant for condensed aromatic systems such as anthracene and phenanthrene, whose extended π-conjugation confers significant UV absorbance that could, in the absence of appropriate dark controls and light-only reference experiments, lead to an overestimation of the true photocatalytic contribution. Unfortunately, the reviewed PAH-specific literature does not consistently report control experiments that isolate these contributions, which precludes definitive quantitative attribution. This situation reflects a broader methodological challenge across AOP-based degradation research: experimental variability encompassing differences in light source type and intensity, catalyst loading, initial pollutant concentration, pH, and the presence or absence of radical scavengers renders direct cross-study comparison of reported efficiencies unreliable in the absence of a common reference framework [88,89]. The absence of field-wide standardized testing protocols remains a fundamental obstacle to drawing generalizable conclusions about photocatalytic performance in PAH remediation systems.

From a translational perspective, the reviewed studies are predominantly conducted under idealized laboratory conditions using synthetic aqueous solutions with single PAH compounds—a common limitation across heterogeneous photocatalysis research, where bench-scale setups under controlled conditions remain the norm rather than the exception [90]. In natural and industrial water matrices, the presence of co-occurring dissolved organic matter, competing inorganic ions, and suspended solids can significantly suppress photocatalytic activity through radical scavenging, active site blocking, and reduced photon penetration [89]. Natural antioxidant systems, including halides and polyphenols ubiquitous in real water matrices, present additional interference pathways that are rarely accounted for in PAH photocatalysis studies [90]. Similarly, while catalyst recyclability is occasionally reported, systematic long-term stability assessments under operationally relevant conditions—including surface deactivation by intermediate byproducts and potential nanoparticle leaching—remain largely absent from the current PAH-specific literature, despite these being recognized as key bottlenecks for real-world implementation [89,90]. Addressing these gaps through standardized benchmark testing protocols and pilot-scale validation represents an essential prerequisite for the practical deployment of metal oxide nanocomposite-based photocatalysis in PAH-contaminated water remediation.

8. Conclusions

From a sustainable chemistry standpoint, the reviewed studies collectively demonstrate that the rational design of metal oxide-based nanocomposites enables a transition from merely pollutant transformation to controlled, energetically favorable mineralization pathways. The consistent formation of quinone-type intermediates at positions 9 and 10 in both anthracene and phenanthrene reveals a predictable oxidative entry point that can be strategically exploited through band-gap engineering and heterojunction design. Importantly, the shift from UV-dependent systems toward sunlight-active catalysts marks a decisive step in reducing the energetic footprint of advanced oxidation processes.

However, future progress must extend beyond degradation percentages and include systematic assessments of catalyst stability, recyclability, potential nanoparticle leaching, and life-cycle environmental impacts. The sustainable deployment of photocatalytic technologies will depend on integrating material science, environmental toxicology, and process engineering into a unified framework. By consolidating mechanistic insights, intermediate identification, and operational optimization trends, this review provides a structured foundation for the development of next-generation photocatalytic platforms aimed at effective PAH elimination under environmentally relevant conditions, thereby contributing

to the broader objective of safeguarding aquatic and soil systems within the paradigm of sustainable development.

Meanwhile, it is necessary to highlight that operational parameters, including pH, catalyst loading, light intensity, and the presence of electron acceptors, play critical roles in optimizing photocatalytic degradation efficiency. Moreover, the synthesis of nanocomposites with tailored properties, such as the incorporation of dopants and the creation of heterojunctions, further enhances photocatalytic performance. Despite significant progress, challenges remain in the scalability, long-term stability, and ecological safety of these nanomaterials.

The improved charge separation, increased surface area, and active sites availability are strong arguments for the practical superiority of these materials. The findings of structural modifications of these nanomaterials, which mitigate issues like rapid recombination of electron-hole pairs, demonstrate a successful application of material design principles to enhance photocatalytic performance, providing a direct link between advanced material engineering and environmental chemistry applications.

Photocatalytic degradation of PAHs is also viable under natural environmental conditions, such as exposure to solar radiation and neutral pH. This aspect is crucial in moving from laboratory-scale experiments to real-world scenarios. The optimal ranges that were identified in this paper can serve as a significant reference point for further research attempting to replicate or scale these processes. The detailed discussion on operational parameters, such as catalyst loading, pH, and light intensity, may represent a basis for some new solutions in the optimization of photocatalytic degradation systems.

Author Contributions: Conceptualization, V.N. and S.A.; writing—original draft preparation, V.N.; writing—review and editing, V.N., S.A. and M.R.; data curation, S.A. and M.R.; supervision—S.A. and M.R. All authors have read and agreed to the published version of the manuscript.

Funding: The research presented in this paper was conducted with the financial support of the Ministry of Science, Technological Development, and Innovations of the Republic of Serbia, within the funding of the scientific research work at the University of Belgrade, Technical Faculty in Bor (contract number 451-03-34/2026-03/200131).

Data Availability Statement: The original contributions presented in the study are included in the article. Further inquiries can be directed to the corresponding author.

Acknowledgments: All photocatalytic degradation schemes of the compounds discussed in this paper were created using BKChem (version 0.13.0), an open-source chemical drawing program. All schemes were created with the great help of our colleague and assistant, Aleksandar Cvetković.

Conflicts of Interest: The authors declare no conflicts of interest.

References

1. Alagić, S.Č.; Maluckov, B.S.; Radojičić, V.B. How can plants manage polycyclic aromatic hydrocarbons? May these effects represent a useful tool for an effective soil remediation? A review. *Clean Technol. Environ. Policy* **2015**, *17*, 597–614. [CrossRef]
2. Muhammed, Y.G.; Shehu, D.; Ya'u, M.; Babandi, A.; Ibrahim, S.; Yakasai, H.M. Biodegradation of anthracene and phenanthrene by Pseudomonas stutzeri (BUK_BTEG1) isolated from petrochemical contaminated soil. *Acta Biol. Marisiensis* **2021**, *5*, 31–46. [CrossRef]
3. Michał, N.; Ewelina, C.; Iwona, R.; Robert, W.; Przemysław, A. Destruction of anthracene and phenanthrene using PDS/UV, one of advanced oxidation processes in terms of degree of destruction and by-products. *Glob. Nest J.* **2023**, *25*, 20–25. [CrossRef]
4. Torri, S.I.; Cabrera, M.N.; Alberti, C. Comparative dissipation of anthracene and phenanthrene in a pristine Typic Hapludoll soil. *Rev. Int. Contam. Ambient.* **2020**, *36*, 711–727. [CrossRef]
5. Shanker, U.; Jassal, V.; Rani, M. Degradation of toxic PAHs in water and soil using potassium zinc hexacyanoferrate nanocubes. *J. Environ. Manag.* **2017**, *204*, 337–348. [CrossRef]
6. Meenu; Rani, M.; Shanker, U. Sunlight-driven degradation of anthracene and naphthalene on robust Cu^{2+} doped ZnO nanoparticles from simulated rainwater: Optimization factors, kinetics, and reusability. *Environ. Sci. Adv.* **2023**, *3*, 249–265. [CrossRef]

7. Verbruggen, E.M.J. *Environmental Risk Limits for Polycyclic Aromatic Hydrocarbons (PAHs)*; RIVM Report 607711007/2012; National Institute for Public Health and the Environment: Bilthoven, The Netherlands, 2012. Available online: https://www.rivm.nl/bibliotheek/rapporten/607711007.pdf (accessed on 15 October 2024).
8. Verbruggen, E.M.J.; van Herwijnen, R. *Environmental Risk Limits for Phenanthrene*; RIVM Letter Report 601357007/2011; National Institute for Public Health and the Environment: Bilthoven, The Netherlands, 2011. Available online: https://rivm.openrepository.com/handle/10029/256205 (accessed on 15 October 2024).
9. U.S. Environmental Protection Agency (USEPA). *Risk-Based Screening Table—Generic Tables*; Regional Screening Level (RSL) Summary Table (TR = 1×10^{-6} and THQ = 1.0); USEPA: Washington, DC, USA, 2024.
10. U.S. Environmental Protection Agency (USEPA). *Anthracene; CASRN 120-12-7*; Integrated Risk Information System (IRIS); USEPA: Washington, DC, USA, 1991. Available online: https://cfpub.epa.gov/ncea/iris/iris_documents/documents/subst/0434_summary.pdf (accessed on 14 April 2025).
11. U.S. Environmental Protection Agency (USEPA). *Phenanthrene; CASRN 85-01-8*; Integrated Risk Information System (IRIS); USEPA: Washington, DC, USA, 1990. Available online: https://cfpub.epa.gov/ncea/iris/iris_documents/documents/subst/0459_summary.pdf (accessed on 14 April 2025).
12. Gupta, S.; Narayan, H.; Jain, R.K. A review of some metal-oxide based nanocomposites for photocatalytic treatment of wastewater. *Adv. Nat. Sci. Nanosci. Nanotechnol.* **2023**, *14*, 013001. [CrossRef]
13. Jiménez-Bautista, K.; Gascó, A.; Ramos, D.R.; Palomo, E.; Muelas-Ramos, V.; Canle, M.; Hermosilla, D.; Bahamonde, A. Solar-assisted photodegradation of pesticides over pellet-shaped TiO_2-kaolin catalytic macrocomposites at semi-pilot-plant scale: Elucidation of photo-mechanisms and water matrix effect. *J. Clean. Prod.* **2023**, *426*, 139203. [CrossRef]
14. Tofa, T.S.; Kunjali, K.L.; Dutta, J.; Paul, S. Visible light photocatalytic degradation of microplastic residues with zinc oxide nanorods. *Environ. Chem. Lett.* **2019**, *17*, 1341–1346. [CrossRef]
15. Jiang, D.; Xue, J.; Wu, L.; Zhou, W.; Zhang, Y.; Li, X. Photocatalytic performance enhancement of CuO/Cu_2O heterostructures for photodegradation of organic dyes: Effects of CuO morphology. *Appl. Catal. B Environ.* **2017**, *211*, 199–204. [CrossRef]
16. Mondal, K. Recent advances in the synthesis of metal oxide nanofibers and their environmental remediation applications. *Inventions* **2017**, *2*, 9. [CrossRef]
17. Allé, P.H.; Adouby, K.; Garcia-Muñoz, P.; Keller, N.; Robert, D. Efficient photocatalytic mineralization of polymethylmethacrylate and polystyrene nanoplastics by TiO_2/β-SiC alveolar foams. *Environ. Chem. Lett.* **2021**, *19*, 1803–1808. [CrossRef]
18. Goktas, S.; Goktas, A. A comparative study on recent progress in efficient ZnO based nanocomposite and heterojunction photocatalysts: A review. *J. Alloys Compd.* **2021**, *863*, 158734. [CrossRef]
19. Raizada, P.; Sudhaik, A.; Singh, P. Photocatalytic water decontamination using graphene and ZnO coupled photocatalysts: A review. *Mater. Sci. Energy Technol.* **2019**, *2*, 509–525. [CrossRef]
20. Basit, M.; Javed, S.; Ali, S.; Qureshi, A.A.; Gul, I.; Akram, M. Recent innovations in low dimensional ZnO nanostructures/nanocomposites for photocatalytic degradation. *Mater. Innov.* **2022**, *2*, 225–254. [CrossRef]
21. Shekofteh-Gohari, M.; Habibi-Yangjeh, A.; Abitorabi, M.; Rouhi, A. Magnetically separable nanocomposites based on ZnO and their applications in photocatalytic processes: A review. *Crit. Rev. Environ. Sci. Technol.* **2018**, *48*, 806–857. [CrossRef]
22. Nemiwal, M.; Zhang, T.C.; Kumar, D. Recent progress in g-C_3N_4, TiO_2, and ZnO based photocatalysts for dye degradation: Strategies to improve photocatalytic activity. *Sci. Total Environ.* **2021**, *767*, 144896. [CrossRef]
23. Ren, Y.; Zeng, D.; Ong, W.J. Interfacial engineering of graphitic carbon nitride (g-C_3N_4)-based metal sulfide heterojunction photocatalysts for energy conversion: A review. *Chin. J. Catal.* **2019**, *40*, 289–319. [CrossRef]
24. Rueda-Marquez, J.J.; Levchuk, I.; Fernández Ibañez, P.; Sillanpää, M. A critical review on application of photocatalysis for toxicity reduction of real wastewaters. *J. Clean. Prod.* **2020**, *258*, 120694. [CrossRef]
25. Kumari, V.; Mittal, A.; Jindal, J.; Yadav, S.; Kumar, N. S-, N- and C-doped ZnO as semiconductor photocatalysts: A review. *Front. Mater. Sci.* **2019**, *13*, 1–22. [CrossRef]
26. Patnaik, S.; Sahoo, D.; Parida, K. Recent advances in anion doped g-C_3N_4 photocatalysts: A review. *Carbon* **2021**, *172*, 682–711. [CrossRef]
27. Kumaravel, V.; Mathew, S.; Bartlett, J.; Pillai, S.C. Photocatalytic hydrogen production using metal doped TiO_2: A review of recent advances. *Appl. Catal. B Environ.* **2019**, *244*, 1021–1064. [CrossRef]
28. Ahmed, S.; Rasul, M.G.; Brown, R.J.; Hashib, M.A. Influence of parameters on the heterogeneous photocatalytic degradation of pesticides and phenolic contaminants in wastewater: A short review. *J. Environ. Manag.* **2011**, *92*, 311–330. [CrossRef] [PubMed]
29. Roushenas, P.; Ong, Z.C.; Ismail, Z.; Majidnia, Z.; Ang, B.C.; Asadsangabifard, M.; Onn, C.C.; Tam, J.H. Operational parameters effects on photocatalytic reactors of wastewater pollutant: A review. *Desalin. Water Treat.* **2018**, *120*, 109–118. [CrossRef]
30. Madhura, L.; Kanchi, S.; Inamuddin; Bisetty, K.; Singh, S.; Sabela, M. *Nanotechnology-Based Water Quality Management for Wastewater Treatment*; Springer International Publishing: Cham, Switzerland, 2019; Volume 17. [CrossRef]
31. Khasawneh, O.F.S.; Palaniandy, P. Photocatalytic degradation of pharmaceuticals using TiO_2 based nanocomposite catalyst: A review. *Civ. Environ. Eng. Rep.* **2019**, *29*, 1–33. [CrossRef]

32. Shah, Z.; Shaheen, K.; Uddin, A.; Khan, S.B.; Salman, S.M.; Arshad, T. Recent and future prospective of various photocatalysts for environmental pollution and energy production: A review. *Surf. Rev. Lett.* **2021**, *28*, 2130002. [CrossRef]
33. Gnanaprakasam, A.; Sivakumar, V.; Thirumarimurugan, M. Influencing parameters in the photocatalytic degradation of organic effluent via nanometal oxide catalyst: A review. *Indian J. Mater. Sci.* **2015**, *2015*, 601827. [CrossRef]
34. Akpan, U.G.; Hameed, B.H. Parameters affecting the photocatalytic degradation of dyes using TiO_2-based photocatalysts: A review. *J. Hazard. Mater.* **2009**, *170*, 520–529. [CrossRef]
35. Thakur, R.; Chaudhary, R.; Singh, C. Fundamentals and applications of the photocatalytic treatment for the removal of industrial organic pollutants and effects of operational parameters: A review. *J. Renew. Sustain. Energy* **2010**, *2*, 042701. [CrossRef]
36. Constantino, D.S.M.; Dias, M.M.; Silva, A.M.T.; Faria, J.L.; Silva, C.G. Intensification strategies for improving the performance of photocatalytic processes: A review. *J. Clean. Prod.* **2022**, *340*, 130800. [CrossRef]
37. Sales, H.B.; Menezes, R.R.; Neves, G.A.; Souza, J.J.N.d.; Ferreira, J.M.; Chantelle, L.; Menezes de Oliveira, A.L.; Lira, H.d.L. Development of Sustainable Heterogeneous Catalysts for the Photocatalytic Treatment of Effluents. *Sustainability* **2020**, *12*, 7393. [CrossRef]
38. Nguyen, V.Q.; Baynosa, M.L.; Nguyen, V.H.; Tuma, D.; Lee, Y.R.; Shim, J.J. Solvent-driven morphology-controlled synthesis of highly efficient long-life ZnO/graphene nanocomposite photocatalysts for the practical degradation of organic wastewater under solar light. *Appl. Surf. Sci.* **2019**, *486*, 37–51. [CrossRef]
39. Hassan, S.S.M.; Azab, W.I.M.E.; Ali, H.R.; Mansour, M.S.M. Green synthesis and characterization of ZnO nanoparticles for photocatalytic degradation of anthracene. *Adv. Nat. Sci. Nanosci. Nanotechnol.* **2015**, *6*, 045012. [CrossRef]
40. Theurich, J.; Bahnemann, D.W.; Vogel, R. Photocatalytic degradation of naphthalene and anthracene: GC–MS analysis of the degradation pathway. *Res. Chem. Intermed.* **1997**, *23*, 247–274. [CrossRef]
41. Nguyen, V.H.; Phan Thi, L.A.; Van Le, Q.; Singh, P.; Raizada, P.; Kajitvichyanukul, P. Tailored photocatalysts and revealed reaction pathways for photodegradation of polycyclic aromatic hydrocarbons (PAHs) in water, soil and other sources. *Chemosphere* **2020**, *260*, 127529. [CrossRef]
42. Chen, H.; Wen, M.; Huang, Z.; Wu, Q.; Liu, J.; Tu, T. Construction of Cu@ZnO nanobrushes based on Cu nanowires and their high-performance selective degradation of polycyclic aromatic hydrocarbons. *J. Mater. Chem. A* **2015**, *3*, 600–607. [CrossRef]
43. Rani, M.; Rachna; Shanker, U. Mineralization of carcinogenic anthracene and phenanthrene by sunlight active bimetallic oxides nanocomposites. *J. Colloid Interface Sci.* **2019**, *555*, 676–688. [CrossRef]
44. Sliem, M.A.; Salim, A.Y.; Mohamed, G.G. Photocatalytic degradation of anthracene in aqueous dispersion of metal oxides nanoparticles: Effect of different parameters. *J. Photochem. Photobiol. A Chem.* **2019**, *371*, 327–335. [CrossRef]
45. Woo, O.T.; Chung, W.K.; Wong, K.H.; Chow, A.T.; Wong, P.K. Photocatalytic oxidation of polycyclic aromatic hydrocarbons: Intermediates identification and toxicity testing. *J. Hazard. Mater.* **2009**, *168*, 1192–1199. [CrossRef] [PubMed]
46. Martínez-Vargas, B.L.; Cruz-Ramírez, M.; Díaz-Real, J.A.; Rodríguez-López, J.L.; Bacame-Valenzuela, F.J.; Ortega-Borges, R.; Reyes-Vidal, Y.; Ortiz-Frade, L. Synthesis and characterization of n-ZnO/p-MnO nanocomposites for the photocatalytic degradation of anthracene. *J. Photochem. Photobiol. A Chem.* **2019**, *369*, 85–96. [CrossRef]
47. Kou, J.; Li, Z.; Guo, Y.; Gao, J.; Yang, M.; Zou, Z. Photocatalytic degradation of polycyclic aromatic hydrocarbons in GaN:ZnO solid solution-assisted process: Direct hole oxidation mechanism. *J. Mol. Catal. A Chem.* **2010**, *325*, 48–54. [CrossRef]
48. Zhao, X.; Cai, Z.; Wang, T.; O'Reilly, S.E.; Liu, W.; Zhao, D. A new type of cobalt-deposited titanate nanotubes for enhanced photocatalytic degradation of phenanthrene. *Appl. Catal. B Environ.* **2016**, *187*, 134–143. [CrossRef]
49. Chauhan, H.A.; Rafatullah, M.; Ali, K.A.; Siddiqui, M.R.; Khan, M.A.; Alshareef, S.A. Metal-based nanocomposite materials for efficient photocatalytic degradation of phenanthrene from aqueous solutions. *Polymers* **2021**, *13*, 2374. [CrossRef]
50. Bai, H.; Zhou, J.; Zhang, H.; Tang, G. Enhanced adsorbability and photocatalytic activity of TiO_2-graphene composite for polycyclic aromatic hydrocarbons removal in aqueous phase. *Colloids Surf. B Biointerfaces* **2017**, *150*, 68–77. [CrossRef]
51. Wen, S.; Zhao, J.; Sheng, G.; Fu, J.; Peng, P. Photocatalytic reactions of phenanthrene at TiO_2/water interfaces. *Chemosphere* **2002**, *46*, 871–877. [CrossRef]
52. Rachna; Rani, M.; Shanker, U. Degradation of tricyclic polyaromatic hydrocarbons in water, soil and river sediment with a novel TiO_2 based heterogeneous nanocomposite. *J. Environ. Manag.* **2019**, *248*, 109340. [CrossRef] [PubMed]
53. Zhao, Z.; Qin, Z.; Xia, L.; Osman, S.; Singh, R.P.; Omer, A.A. Cu/N-codoped TiO_2 prepared by the sol–gel method for phenanthrene removal under visible light irradiation. *Environ. Sci. Pollut. Res.* **2020**, *27*, 17530–17540. [CrossRef] [PubMed]
54. Nedelkovski, V.; Radovanović, M.; Antonijević, M. Advances in Photocatalytic Degradation of Crystal Violet Using ZnO-Based Nanomaterials and Optimization Possibilities: A Review. *ChemEngineering* **2025**, *9*, 120. [CrossRef]
55. Qiu, T.; Chen, G. Degradation of Naphthalene and Anthracene Using the CdS/ZnO with Enhanced Photocatalytic Activities. *Environ. Technol. Innov.* **2024**, *36*, 103741. [CrossRef]
56. Chauhan, H.A.; Rafatullah, M.; Ali, K.A.; Umar, M.F.; Khan, M.A.; Jeon, B.-H. Photocatalytic Activity of Graphene Oxide/Zinc Oxide Nanocomposite Derived from Rice Husk for the Degradation of Phenanthrene under Ultraviolet-Visible Light. *J. Water Process Eng.* **2022**, *47*, 102714. [CrossRef]

57. Huang, J.; Zhou, T.; Zhao, W.; Cui, S.; Guo, R.; Li, D.; Kadasala, N.R.; Han, D.; Jiang, Y.; Liu, Y.; et al. Multifunctional Magnetic Fe_3O_4/Cu_2O-Ag Nanocomposites with High Sensitivity for SERS Detection and Efficient Visible Light-Driven Photocatalytic Degradation of Polycyclic Aromatic Hydrocarbons (PAHs). *J. Colloid Interface Sci.* **2022**, *628*, 315–326. [CrossRef]
58. Dutta, V.; Devasia, J.; Chauhan, A.; M, J.; L, V.V.; Jha, A.; Nizam, A.; Lin, K.-Y.A.; Ghotekar, S. Photocatalytic Nanomaterials: Applications for Remediation of Toxic Polycyclic Aromatic Hydrocarbons and Green Management. *Chem. Eng. J. Adv.* **2022**, *11*, 100353. [CrossRef]
59. Wei, R.; Ge, Y.; Meng, H.; Huang, G.; Wu, J.; Wen, F.; Liu, H.; Shen, X. Enhanced Photocatalytic Degradation of Polycyclic Aromatic Hydrocarbons (PAHs) in Biochar Using Nano-TiO2 under Ultraviolet Light Irradiation: Effect and Mechanisms. *Chem. Eng. J.* **2025**, *503*, 158352. [CrossRef]
60. Wadaan, M.A.; Baabbad, A.; Yesuf, M.B.; Asaithambi, P. Kinetics Analysis of PAHs Degradation Using SiO_2–ZnO Nanoparticles and Evaluating Their Antibacterial and Antibiofilm Efficacy. *Environ. Res.* **2024**, *260*, 119669. [CrossRef] [PubMed]
61. Xiao, X.; Zhai, S.; Wang, J.; Wang, M.; Huang, M.; Tao, Y.; Wang, H.; Xiong, J.; Wang, C.; Liang, Y. In Situ Analysis of Oxygen Vacancy Modified TiO_2-Ov/G-C_3N_4 S-Scheme Heterojunction by 2D-PCIS Spectroscopy for Efficient Synergistic Photocatalytic Degradation of Naphthalene in Water. *Environ. Res.* **2025**, *284*, 122231. [CrossRef]
62. de Jesús González Terán-Espinoza, A.; Lopez-Lopez, A.; Alvarez-Amparán, M.A.; Cedeño-Caero, L.; Mendoza-Nieto, J.A. Visible-Light-Driven Degradation of Phenanthrene in the Presence of Metal-Doped Lithium Titanate Photocatalysts in Water Matrixes. *Top. Catal.* **2025**, *68*, 1639–1651. [CrossRef]
63. Wang, J.; Luo, Z.; Song, Y.; Zheng, X.; Qu, L.; Qian, J.; Wu, Y.; Wu, X.; Wu, Z. Remediation of Phenanthrene Contaminated Soil by G-C3N4/Fe3O4 Composites and Its Phytotoxicity Evaluation. *Chemosphere* **2019**, *221*, 554–562. [CrossRef]
64. Brindhadevi, K.; Kim, P.T.; AlSalhi, M.S.; Abd Elkader, O.H.; T, N.; Lee, J.; Bharathi, D. Deciphering the Photocatalytic Degradation of Polyaromatic Hydrocarbons (PAHs) Using Hausmannite (Mn_3O_4) Nanoparticles and Their Efficacy against Bacterial Biofilm. *Chemosphere* **2024**, *349*, 140961. [CrossRef]
65. Azim, M.B.; Arafat, M.I.; Nargis, F.; Dhar, S.A.; Qadir, M.R.; Gafur, M.A.; Gulshan, F. Effect of Dissolved Oxygen Content on Photocatalytic Performance of Graphene Oxide. *J. Nanotechnol. Res.* **2024**, *6*, 6–15. [CrossRef]
66. Rubio-Clemente, A.; Chica, E.; Peñuela, G. Evaluation of the UV/H_2O_2 System for Treating Natural Water with a Mixture of Anthracene and Benzo[A]Pyrene at Ultra-Trace Levels. *Environ. Sci. Pollut. Res.* **2018**, *26*, 4381–4392. [CrossRef]
67. Kavitha, R.; Archana, K.M.; Rajagopal, R. GCMS Investigation of Sunlight-Driven Photocatalytic Breakdown of Naphthalene and Anthracene Employing Nano Ceria. *Catal. Today* **2026**, *470*, 115754. [CrossRef]
68. Rubio-Clemente, A.; Torres-Palma, R.A.; Peñuela, G.A. Removal of Polycyclic Aromatic Hydrocarbons in Aqueous Environment by Chemical Treatments: A Review. *Sci. Total Environ.* **2014**, *478*, 201–225. [CrossRef] [PubMed]
69. Abd Manan, T.S.B.; Khan, T.; Sivapalan, S.; Jusoh, H.; Sapari, N.; Sarwono, A.; Ramli, R.M.; Harimurti, S.; Beddu, S.; Sadon, S.N.; et al. Application of Response Surface Methodology for the Optimization of Polycyclic Aromatic Hydrocarbons Degradation from Potable Water Using Photo-Fenton Oxidation Process. *Sci. Total Environ.* **2019**, *665*, 196–212. [CrossRef]
70. Zheng, B.; Zhong, J.; He, J.; Ren, X. Degradation Kinetics, Influencing Factors, and Mechanisms of Polycyclic Aromatic Hydrocarbons in a Fe3O4-NZVI Fenton-like System. *Desalin. Water Treat.* **2024**, *320*, 100844. [CrossRef]
71. Bendouz, M.; Tran, L.H.; Coudert, L.; Mercier, G.; Blais, J.-F. Degradation of Polycyclic Aromatic Hydrocarbons in Different Synthetic Solutions by Fenton's Oxidation. *Environ. Technol.* **2016**, *38*, 116–127. [CrossRef]
72. Karam, F.F.; Hussein, F.H.; Baqir, S.J.; Halbus, A.F.; Dillert, R.; Bahnemann, D. Photocatalytic Degradation of Anthracene in Closed System Reactor. *Int. J. Photoenergy* **2014**, *2014*, 503825. [CrossRef]
73. Wang, M.; Li, T.; Hou, Q.; Hao, Y.; Wang, Z. Facile One-Step Preparation of Co and CE Doped TiO_2 in Visible Light Pms Activation for Pahs Degradation. *SSRN Electron. J.* **2022**, *308*, 136360. [CrossRef]
74. Fischer, A.F.; Bahry, T.; Xie, Z.; Batista da Silva Junior, R.; Qian, K.; Li, R.; Kwan, J.; Jerome, F.; Valange, S.; Liu, W.; et al. The Roles of Hydroxyl Radicals and Superoxide in Oxidizing Aqueous Benzyl Alcohol under Ultrasound Irradiation. *ChemSusChem* **2024**, *18*, e202500097. [CrossRef]
75. Guo, Y.; Yu, G.; von Gunten, U.; Wang, Y. Evaluation of the Role of Superoxide Radical as Chain Carrier for the Formation of Hydroxyl Radical during Ozonation. *Water Res.* **2023**, *242*, 120158. [CrossRef] [PubMed]
76. St. Mary, L.; Trine, L.S.D.; Roper, C.; Wiley, J.; Massey Simonich, S.L.; McCoustra, M.; Henry, T.B. Time-Related Alteration of Aqueous-Phase Anthracene and Phenanthrene Photoproducts in the Presence of TiO_2 Nanoparticles. *Environ. Sci. Technol.* **2021**, *55*, 3727–3735. [CrossRef]
77. Qiao, M.; Liu, B.; Zhao, X.; Gong, Y.; Wang, Y.; Cao, W. Formation of Oxygenated Polycyclic Aromatic Hydrocarbons by Photoelectrocatalysis Using TiO_2 Nanotubes. *RSC Adv.* **2017**, *7*, 51678–51686. [CrossRef]
78. Qu, J.; Pei, L.; Wang, X.; Fu, S.; Yong, L.; Xiao, X.; Xie, Q.; Fan, B.; Song, Y. Acute and Subchronic Oral Toxicity of Anthraquinone in Sprague Dawley Rats. *Int. J. Environ. Res. Public Health* **2022**, *19*, 10413. [CrossRef]

79. Carl Roth GmbH + Co. KG. Safety Data Sheet According to Regulation (EC) No. 1907/2006 (REACH), Product: Anthraquinone ROTI®CALIPURE, Article Number: 9754. Version 7.0. 2024. Available online: https://www.carlroth.com/medias/SDB-9754-MT-EN.pdf?context=bWFzdGVyfHNlY3VyaXR5RGF0YXNoZWV0c3wyNzIyOTd8YXBwbGljYXRpb24vcGRmfGFHSXdMMmd4T0M4NU1qWTBOVGsyTURJMU16YzBMMU5FUWw4NU56VTBYMDFVWDBWT0xuQmtaZ3xjMWQwMGM4NmQ5OTE4M2NlMWUzMzlkMzYwMjU4ZDY1YjdkOGNmZDRhMjU3NTUxOTA3MDYwOGRiOTUzNGI0NTk4 (accessed on 2 April 2026).
80. Tukaj, Z.; Aksmann, A. Toxic Effects of Anthraquinone and Phenanthrenequinone upon Scenedesmus Strains (Green Algae) at Low and Elevated Concentration of CO_2. *Chemosphere* **2007**, *66*, 480–487. [CrossRef]
81. Carl Roth GmbH + Co. KG. Safety Data Sheet According to Regulation (EC) No. 1907/2006 (REACH), Product: Anthrone p.a., Article Number: 2673. Version 6.0. 2022. Available online: https://www.carlroth.com/medias/SDB-2673-DE-EN.pdf?context=bWFzdGVyfHNlY3VyaXR5RGF0YXNoZWV0c3wyNTU0NTB8YXBwbGljYXRpb24vcGRmfGFEUXdMMmcwTkM4NU1qQTJOalUxTWpJeE56a3dMMU5FUWw4eU5qY3pYMFJGWDBWT0xuQmtaZ3w4NDcxNDU4NDAxODc3Y2YxN2YwYmIzODYzNjMwMDQxMDQyOTg0Njg1M2IyNTE5N2NmMjEyZmI0YTFmNzhkMzI0 (accessed on 2 April 2026).
82. Long, F.; Ren, Y.; Ji, Y.; Li, J.; Zhang, H.; Wu, Z.; Gao, R.; Bi, F.; Liu, Z.; Li, H. Pollution Characteristics, Toxicological Properties, and Health Risk Assessment of Phthalic Acid Esters in Water, Soil, and Atmosphere. *Atmosphere* **2024**, *15*, 1071. [CrossRef]
83. Sokołowski, A.; Kończak, M.; Oleszczuk, P.; Gao, Y.; Czech, B. Environmental and Food Contamination by Phthalic Acid Esters (PAEs): Overview. *Water Air Soil Pollut.* **2024**, *235*, 313. [CrossRef]
84. JRC. *European Union Risk Assessment Report—Bis (2-ethylhexyl) phthalate (DEHP)*; JRC Publications Repository: Brussels, Belgium. Available online: https://publications.jrc.ec.europa.eu/repository/handle/JRC45705 (accessed on 14 April 2026).
85. Loba Chemie Pvt. Ltd. Safety Data Sheet: 3-Hydroxy-2-naphthoic acid, Product Code 04127. Version 1.0. 2022-04-15. Available online: https://www.lobachemie.com/lab-chemical-msds/MSDS-3hydroxy2naphthoic-acid-CASNO-92-70-04127-EN.aspx (accessed on 4 April 2026).
86. Kang, H.J.; Jung, Y.; Kwon, J.-H. Changes in Ecotoxicity of Naphthalene and Alkylated Naphthalenes during Photodegradation in Water. *Chemosphere* **2019**, *222*, 656–664. [CrossRef]
87. Cosmetic Ingredient Review Expert Panel. Final Report on the Safety Assessment of Maleic Acid1. *Int. J. Toxicol.* **2007**, *26*, 125–130. [CrossRef] [PubMed]
88. Anisuzzaman, S.M.; Joseph, C.G.; Pang, C.K.; Affandi, N.A.; Maruja, S.N.; Vijayan, V. Current Trends in the Utilization of Photolysis and Photocatalysis Treatment Processes for the Remediation of Dye Wastewater: A Short Review. *ChemEngineering* **2022**, *6*, 58. [CrossRef]
89. Paiu, M.; Lutic, D.; Favier, L.; Gavrilescu, M. Heterogeneous Photocatalysis for Advanced Water Treatment: Materials, Mechanisms, Reactor Configurations, and Emerging Applications. *Appl. Sci.* **2025**, *15*, 5681. [CrossRef]
90. Younis, S.A.; Kim, K.-H. Heterogeneous Photocatalysis Scalability for Environmental Remediation: Opportunities and Challenges. *Catalysts* **2020**, *10*, 1109. [CrossRef]

Disclaimer/Publisher's Note: The statements, opinions and data contained in all publications are solely those of the individual author(s) and contributor(s) and not of MDPI and/or the editor(s). MDPI and/or the editor(s) disclaim responsibility for any injury to people or property resulting from any ideas, methods, instructions or products referred to in the content.